CRITICAL REVIEW

Laser powder bed fusion of the steels used in the plastic injection mould industry: a review of the influence of processing parameters on the final properties

Ângela Cunha[1,2] · Ana Marques[1,2] · Mariana Rodrigues Silva[1] · Flávio Bartolomeu[1,2] · Filipe Samuel Silva[1,2] · Michael Gasik[3] · Bruno Trindade[4] · Óscar Carvalho[1,2]

Abstract

This review provides a critical overview of the influence of the laser powder bed fusion (LPBF) processing parameters on the final properties of the three steels used in the plastic injection mould industry (420 stainless steel, H13, and P20 steels). The main objective is to provide an engineering overview concerning the response of the parts made from the materials produced by this technique. A comprehensive summary of LPBF processing parameters and their influence on the physical, mechanical, tribological, corrosion, and thermal properties of the LPBFed parts is presented and discussed. An analysis of the suitability of these steels for the production of components for the plastic injection mould industry is also presented. This review shows that, despite the increase research about these steels over recent years, there are still some shortcomings and issues that require further investigation, such as the behaviour of LPBFed parts in-service conditions, their thermal behaviour, and the influence of the processing parameters and their surroundings on the final properties of the parts.

Keywords Laser powder bed fusion · 420 stainless steel · H13 and P20 steels · Final properties · Plastic injection mould industry

1 Introduction

Additive manufacturing (AM) has gained considerable interest during the last few decades [1–5]. In contrast to subtractive techniques, AM involves a family of layer-by-layer building technologies capable of producing geometrically intricate components in a single step [1, 2, 6–11]. AM has several advantages compared to traditional methods of manufacturing, such as the (i) manufacture of components with highly complex geometries, (ii) improvement of the production-development cycle, (iii) ability to fabricate small batches of parts in a short time, with low financial investment, (iv) use of a wide range of materials, (v) cost saving by optimising material usage (low waste of material), (vi) production of functionally graded parts, and (vii) customisation without requiring extremely expensive tools and systems [5, 7, 12–14]. These advantages make AM attractive for a wide range of fields including the aerospace, biomedical, automobile, and mould industries [3, 5, 15, 16].

AM techniques can be categorised based on their type of feedstock (powder or wire) and the energy source employed (laser or electron beam) [14, 17, 18]. Laser powder bed fusion (LPBF) is considered one of the most promising additive manufacturing technologies in different fields of the industry, such as aerospace, automotive, and injection moulds [2, 3, 19, 20]. This technique uses a high-energy laser beam to melt a bed of metal powder, in a protective atmosphere along the laser path, which rapidly solidifies. The process is then repeated for successive layers until the three-dimensional components required are built completely [14, 19, 21–23]. LPBF includes complex processes that

✉ Ângela Cunha
  a.cunha@dem.uminho.pt

1 CMEMS – Center for Microelectromechanical Systems, University of Minho, Guimarães, Portugal

2 LABBELS – Associate Laboratory, Braga/Guimarães, Portugal

3 School of Chemical Engineering, Aalto University Foundation, Espoo, Finland

4 CEMMPRE – Center for Mechanical Engineering, Materials and Processes, University of Coimbra, Coimbra, Portugal

involve the understanding of different parameters related to the material, machine, and manufacturing [21]. A wide variety of metal powders have been fabricated by LPBF, including Al-based, Ti-based, Fe-based, Ni-based, Cu-based, and Co-based alloys [24, 25]. The process parameters that most influence the quality and properties of the parts produced, are divided into four categories: (i) laser-related (power, spot size, mode-pulsed or continuous), (ii) scan-related (speed, spacing, pattern), (iii) powder-related (particle size, shape, and distribution, powder bed density, layer thickness, and powder properties), and (iv) temperature-related (powder bed temperature, powder feeder temperature, and temperature uniformity) [17, 26].

The plastic injection moulding industry is one of the fastest-growing industries in the world since a lot of products that are used in daily life involve the use of plastics [27–29]. Despite having numerous advantages, namely high dimensional and geometric precision, repeatability, and adaptability to a wide range of raw materials [30, 31], the costs associated with the mould and the injection machine are high [32, 33]. Therefore, a reduction in cycle time, more specifically the cooling time, has been a never-ending challenge for manufacturing plants, with a direct influence on the production costs, productivity, and quality of the parts produced [29, 34–36]. The use of conformal cooling channels has been one of the main solutions to achieve this objective [37, 38]. In the last few decades, additive manufacturing processes, particularly LPBF, have been widely used in the fabrication of parts and tools with high geometric complexity, challenging the traditional design guidelines for cooling systems in industrial heat transfer cases, namely in the plastic injection moulding industry [39–42]. In fact, this technology allows several innovative design approaches to intricate cooling systems in mould inserts, which cannot be manufactured by conventional machining processes [36, 41], eliminating some limitations associated with the geometric aspects of the mould's cavity and core [43, 44].

Steel alloys are the main materials used for the fabrication of moulds for plastics. They can combine the most essential characteristics required from a mould, in order not to fail in service, e.g., high resistance to corrosion, mechanical resistance, hardness, wear resistance, and resistance to fatigue [31, 45–48]. 420 stainless steel, H13 and P20 steels are the steels most used for the production of moulds for plastics [49–52]. 420 stainless steel is a martensitic low carbon steel (< 0.15 wt% C), with a minimum chromium content of 12%. It is characterized by high strength, hardness, and corrosion properties [33, 53–55]. H13 steel has 0.32–0.45 wt% C, and chromium (4.75–5.50 wt%), molybdenum (1.10–1.75 wt%), silicon (0.80–1.20 wt%), and vanadium (0.80–1.20 wt%) as its main alloying elements. It presents a high tensile strength, hardness, and thermal fatigue [45, 56, 57]. Finally, P20 steel has 0.28–0.4 wt% C, and chromium (1.40–2.00 wt%) and

molybdenum (0.30–0.55 wt%) as its main alloying elements. It is characterized by high toughness, and reasonable hardness, and tensile strength [47, 58, 59].

The present review provides a comprehensive overview of the densification, microstructure, quality of surface finish, and mechanical, corrosion, tribological and thermal properties reported for steels used in the plastic injection moulds produced by LPBF, and their relationship with the processing parameters (Fig. 1).

2 LPBF—powder bed system

AM systems can be divided into three broad categories: (i) wire feed systems, (ii) powder feed systems, and (iii) powder bed systems, in which LPBF is included [18, 60]. A 3D CAD model is imported to the LPBF software system, a laser beam with a high-energy density scans over the layer using the parameters previously defined, and after successive layers a final part is obtained (Fig. 2) [7, 20, 21, 61].

LPBF is a complex process that involves the understanding of different parameters related to the material, machine, and manufacturing aspects. Regarding the material, the powder's properties can be subdivided into multiple levels: (i) physical and chemical properties of the individual particles (morphology, particle size distribution, impurities, composition, moisture, and particle density), (ii) behaviour of the powder ensemble as a whole (apparent density, tap density Hausner ratio, and flowability of powder), and (iii) behaviour of the powder under process-specific conditions (reproducibility, layer density, continuity, and homogeneity). The sum of the various aspects of each level influences the characteristics of the final part, namely density, surface roughness, mechanical properties, and accuracy [63]. Concerning manufacturing, the main relevant and influential processing parameters for LPBF are laser power, scan speed, hatching spacing, and layer thickness (Fig. 3).

The volumetric energy density (VED) (J/mm^3) makes the comparison of parts produced using LPBF under different sets of parameters possible [7, 64]. It can be calculated according to the following equation:

$$\text{VED} = \frac{P}{v \times h \times t} \tag{1}$$

where P is the laser power (W), v represents the scan speed (mm/s), h denotes the hatch spacing (mm), and t is the layer thickness (mm). If the VED is too low, a lack of fusion between the powder particles occurs; if the VED is too high, an excessive evaporation occurs for the parts, which leads to internal porosity [4, 65–69].

Other important aspects of LPBF technique are related to the atmosphere, platform, supports, and scan strategy. The
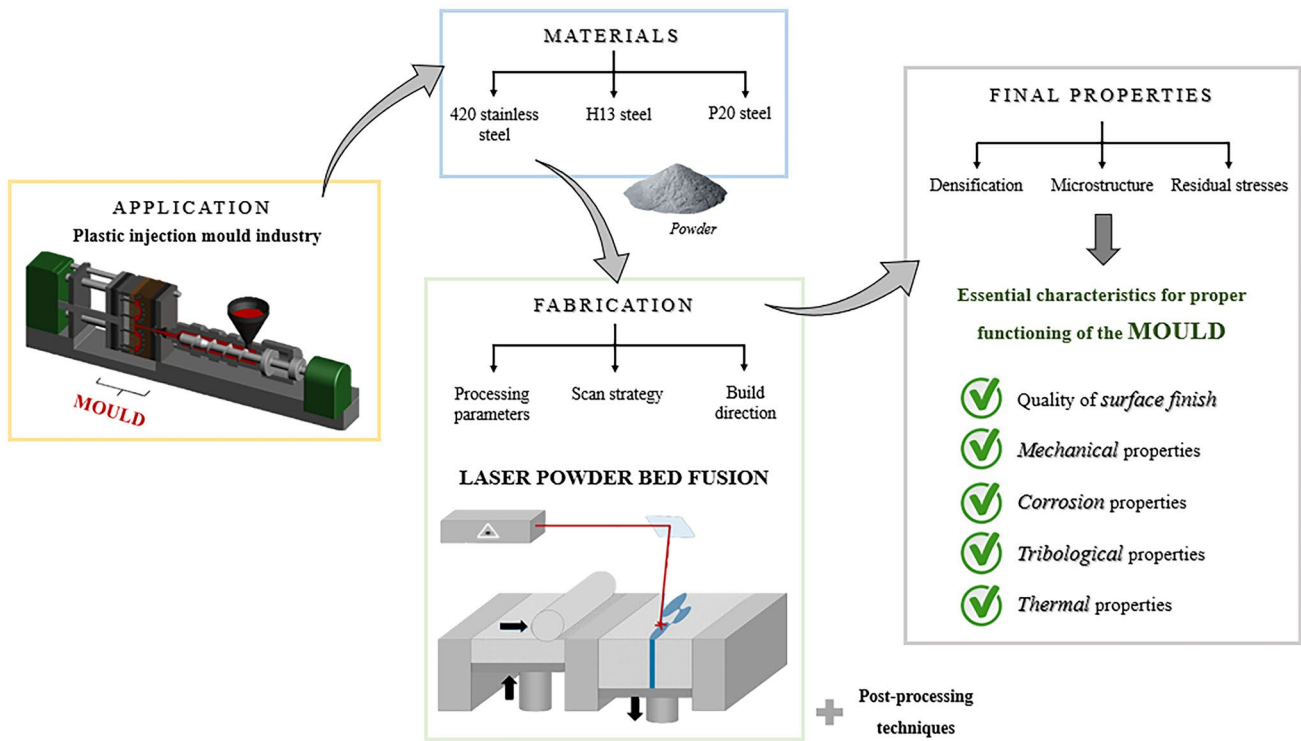
Fig. 1 Structure of this review: a comprehensive overview of the final properties of the steels used in the plastic injection moulds produced by LPBF and their relationship with the processing parameters

material to be produced must be taken into consideration when choosing the atmosphere in order to prevent oxidation. When the powder bed interacts with the laser beam, its temperature increases, and the formation of oxides is likely to occur. To avoid oxidation, the purity of the atmosphere required is generally established by flushing the selected gas into the process chamber, which results in a dilution of the oxygen and impurities initially present [70, 71]. The second important aspect is associated with the temperature of the platform (base plate), which may significantly affect the final

properties of the parts. One of the main issues of LPBF is related to significant thermal stresses resulting from high thermal gradients. This issue can, potentially, be solved by elevating the temperature of the platform during the fabrication, hence reducing temperature gradients during the process [72, 73]. The supports to connect the platform to the parts are extremely important to ensure a good heat transfer during the process, to avoid localised heat accumulation, and to prevent defects in the parts produced [74]. Finally, the laser scan strategy is another important parameter of
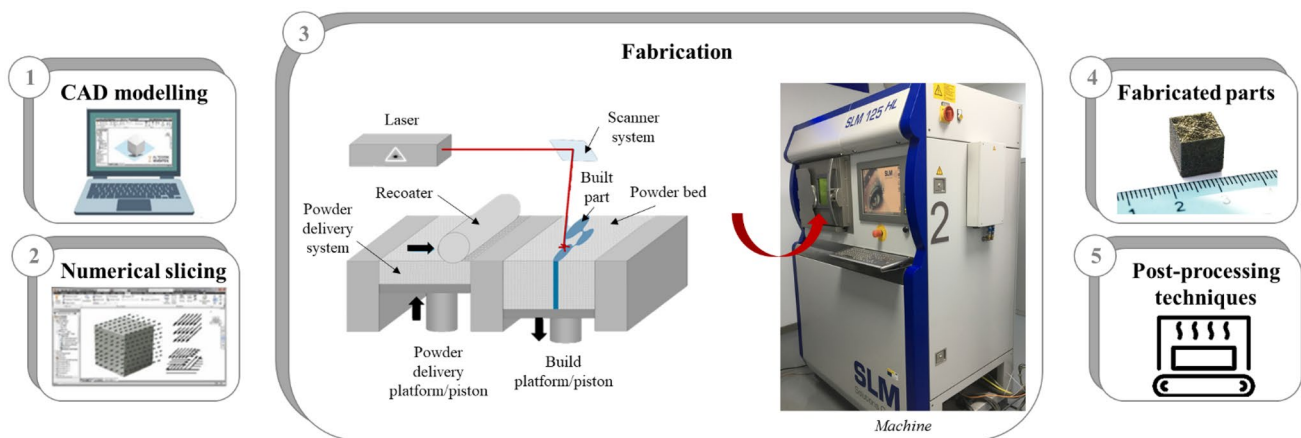
Fig. 2 Schematic representation of the LPBF process (based on [62])

Fig. 3 Schematic diagram of the main processing parameters of the LPBF process (adapted from [7])
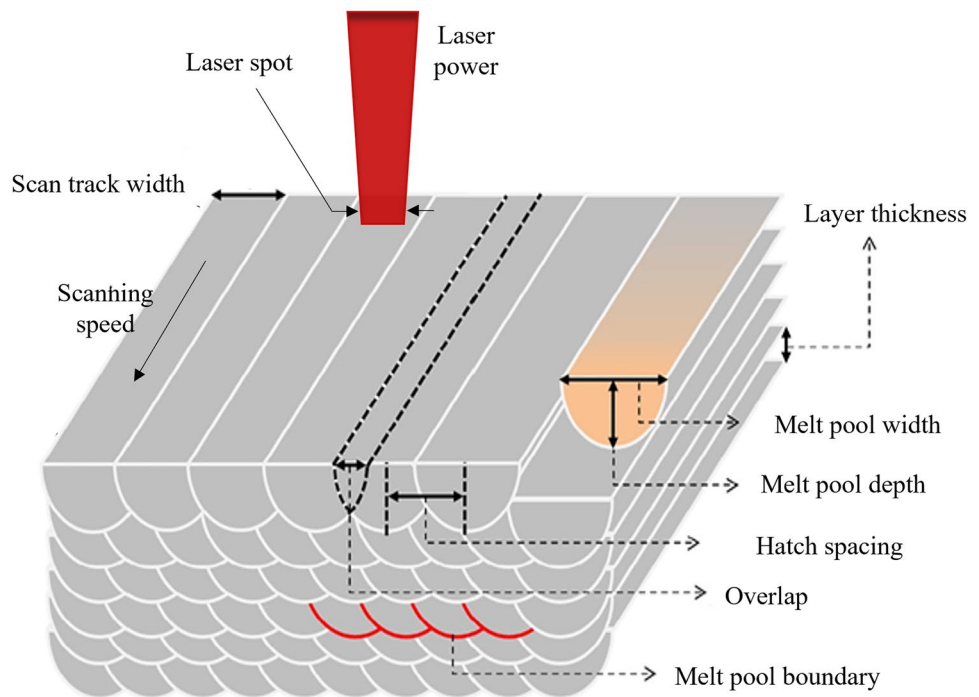
LPBF. It is known that it has a significant impact on the thermal gradient and, consequently, on the formation of the grain structure and crystallographic texture [75, 76]. Zhang et al. [77] and Robinson et al. [78] demonstrated that the 90° rotation of the scan direction after finishing one layer caused a more uniform and lower residual stress compared with no layer rotation, because the perpendicular laser trajectories between each layers balance the directional residual stresses (Fig. 4a). Moreover, this strategy slows down the cooling speed and thus mitigate the residual stress. Thijs et al. [79] concluded that the rotation between successive layers also improved the density of LPBFed parts. On the other hand, Masoomi et al. [80] showed that island scanning is an effective strategy to reduce the final component residual stress, due to the decrease in localised thermal gradients (Fig. 4b).

Therefore, appropriate control of this parameter can significantly improve the heat transfer, leading to the.

formation of homogeneous microstructures, with better final mechanical properties of the parts [75, 81].

3 LPBF process parameters and raw materials

As mentioned previously, 420 stainless steel, and H13 and P20 steels are three of the steel alloys most used in the plastic injection mould industry. The final properties of the LPBFed parts depend on the production equipment and the processing parameters. In this subsection, an overview of the literature on laser powder bed fusion of these steels is presented, which is a tool that can be used by engineers to

Fig. 4 Examples of laser scanning strategies: **a** parallel scanning with and without rotation between successive layers, and **b** island scanning (based on [82, 83])

(a)   **(b)**
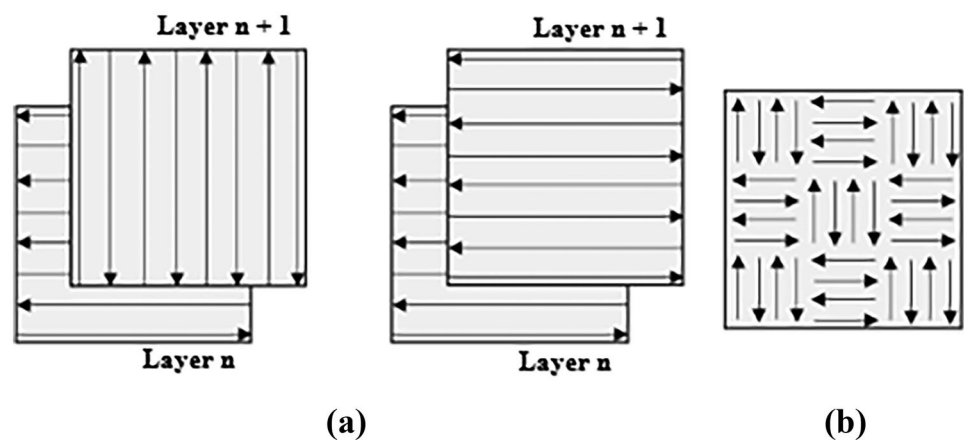
support future works in the scope of the development of parts of these materials produced by this technology.

3.1 420 stainless steel

Most of the studies selected on the use of this steel for the fabrication of moulds by LPBF are quite recent (ten published in 2019–2021 [84–93] and three in 2015 [50, 53, 94]). An overview of the inputs discussed.

in these studies, which are essential for the discussion of the LPBF process, is presented in Table 1. Concerning the LPBF apparatus, the Concept Laser Mlab cusing R machine has been one of the most used [89, 91–93]. Most of the studies concern the production of parts with a simple geometry (cubic shape) [50, 85, 86, 89–94] from spherical particles with an average particle size of between 20 and 53 µm [53, 85, 88–91, 93, 94]. In LPBF, the metal particles need to be spread on the substrate by a continuous and smooth powder transporting process, which requires a high degree of sphericity, and an appropriate particle size distribution to ensure good flowability. The energy density values reported varied from 41.7 to 139.0 J/mm^3, the 63.0 J/mm^3 value being the one most widely used [86, 89, 91–93]. All the studies refer to a layer thickness of between 10 and 50 µm (20 µm is the value most referred [53, 86, 89–93]), and laser power values from 50 to 200 W (most studies opted for 90 W [86, 89, 91–93]).

Regarding scanning speed, most of the studies used 600 to 700 mm/s [53, 86, 88–93]. However, there are two studies that opted for a different approach with lower scanning speed (120 mm/s), and laser power (60 W) [50, 94]. Finally, all the studies indicate hatch spacing values between 80 and 200 µm. Concerning the production strategy, three different approaches have been used: an island pattern with an alternating path, a continuous line scan alternating layers at −45 and +45°, and a rescanning strategy [84, 85, 87, 89, 91–93].

3.2 H13 steel

Among the three steels of this study, H13 has been the most studied to produce parts by LPBF, with thirty-one studies considered in this review, from 2016 to 2021 (Table 2). As for 420 stainless steel, almost all the studies used spherical particles (average diameter sizes from 15 to 63 µm) for the production of cube parts [57, 66, 69, 95–112]. The energy density varied from 17.4 to 760 J/mm^3, with the most reported values of 67, 80, 100, and 300 J/mm^3 [15, 57, 66, 69, 74, 96, 97, 100, 103, 109–116]. In most studies the layer thickness was 30 µm [15, 57, 74, 101, 108, 109, 112–117]. Jung et al. [99] used a dual scan approach, with a layer thickness of 250 µm. In regard to laser power, a wide range of values were reported (90 to 1000 W), with the value of 175 W being the most preferred [15, 57, 74, 109, 112, 114–116,

118]. This value is higher than that used in most cases for 420 stainless steel. Regarding the scanning speed, the literature refers to values in the range of 56 to 1400 mm/s with many studies reporting values similar to the ones for 420 stainless steel (720 mm/s) [15, 74, 109, 111, 112, 114–116]. The hatch spacing used in most of the studies was 120 µm. However, two studies present extremely different values for this parameter (700 and 800 µm) which can be explained by the use of more powerful lasers and/or different scan strategies (dual scan) [99, 106]. The most used scanning strategy was the alternate-hatching pattern and stripe scanning [15, 66, 74, 97, 98, 100, 102, 103, 107, 110, 111, 114, 118].

3.3 P20 steel

The production of P20 steel parts by LPBF has not been studied much yet. Just three studies are included in this review [115, 120, 121], all related to the last 3 years. As for the previous cases, Table 3 presents the inputs of the LPBF process for P20 steel.

Again, these studies mainly concerned the production of cubic parts from spherical particles with an average size from 25 to 70 µm. The energy densities used were similar to the ones of 420 stainless steel and H13 steel (78.0 to 333.1 J/mm^3). In all these studies, the layer thickness was 30 µm and the laser power varied from 100 to 200 W. Two studies used a scanning speed of 800 mm/s [115, 120], and one, 350 mm/s [121]. The hatch spacings chosen were in the range of 80–105 µm. Only one study refers to the scanning strategy adopted (zig-zag strategy) [120].

4 The influence of the LPBF process parameters on the properties of the LPBFed steel parts

In this subsection, the influence of the LPBF process parameters on the densification, microstructure, quality of surface finish, mechanical, corrosion, tribological, and thermal properties of the final parts is presented and discussed. These properties are essential in a plastic injection mould, not only to ensure the smooth operation of the mould in production but also to achieve a good quality of the plastic components produced.

4.1 Densification

The densification of parts in the LPBF process is not just influenced by the energy density collectively, but also by the: laser power, scanning speed, hatch spacing, and layer thickness individually [91]. Fully densified components with the lowest energy density possible are required to avoid any adverse effects of a high energy density such as internal porosity and high surface roughness.

Table 1 Overview of the inputs of the LPBF process for the production of 420 stainless steel parts

First author, year	Powder parameters		Laser parameters			Scan parameters			Other parameters	LPBF machine	Part's geometry/ dimensions
	Particle shape	PSD (μm)	Layer thickness (μm)	Laser power (W)	Spot size (μm)	Scan speed (mm/s)	Scan spacing Hatch spacing (μm)	Scan pattern			
Yang et al. 2021 [84]	---	10–88	50	400	100 200 300 400	1000	80	Island pattern with alternating path	VED: 80, 40, 26.7, 20 J/mm^3 Platform: 95 °C	LPM325 Yb fibre laser	---
Tian et al. 2021 [85]	Spherical	15–60	30	240–280	---	1000–1200	80–120	Zig-zag stripe	Atmosphere: argon VED: 75–85 J/mm^3	EOS M290	Cubes (10×10×10 mm)
Nath et al. 2021 [86]	---	D50-12 D50-28	20	90	---	600	120	---	VED: 29, 38, 48, 63, 75 J/mm^3 Platform: 95 °C	GE Concept Laser Mlab machine	Cubes (10×10×10 mm)
Shen et al. 2020 [87]	---	10–53	50	400	200	700	200	Island pattern with alternating path	Platform: 180 °C	OPM250L Yb fibre laser	---
Shi et al. 2020 [88]	Spherical	D10-19 D50-32 D90-55	30	200	---	600	115	---	Atmosphere: oxygen concentration below 100 ppm	Renishaw AM250 Pulse laser source MP: 400 W	---
Nath et al. 2020 [89]	Spherical	D10-17 D50-28 D90-47	10 20 30	70 90*	---	600* 800 1000	90 120*	Continuous line scan varying between −45° and 45°	Atmosphere: argon	Concept Laser Mlab cusing R machine Yb fibre laser λ: 1050 nm MP: 100 W	Cubes (10×10×10 mm^3)
Saeidi et al. 2019 [90]	Spherical	20–53	20	195	70	700	100	---	VED: 139.0 J/ mm^3	EOS M270 Yb fibre laser MP: 200 W	Cubes (10×10×5 mm^3) Rods (40×4×1 mm^3)
Nath et al. 2019 [93]**	Spherical	D10-17 D50-28 D90-48 (49 for powder with Nb and Mo)	20	90	50	600	120	Line pattern with alternating layers at −45° and +45°	Atmosphere: argon (oxygen content − 0.1 −0.4%) Platform: mild steel VED: 63.0 J/ mm^3	Concept Laser Mlab cusing R machine Yb fibre laser λ: 1050 nm MP: 100 W	Cubes (10×10×10 mm^3)

Table 1 (continued)

First author, year	Powder parameters		Laser parameters			Scan parameters			Other parameters	LPBF machine	Part's geometry/ dimensions
	Particle shape	PSD (µm)	Layer thickness (µm)	Laser power (W)	Spot size (µm)	Scan speed (mm/s)	Scan spacing Hatch spacing (µm)	Scan pattern			
Momenzadeh et al. 2019 [92]**	---	D10–17 D50–28 D90–47	10 (SS420) 20 (SS420 and SS420+)	90	---	600	120	Continuous line laser scan pattern (−45° and 45°)	Atmosphere: argon	Concept Laser Mlab cusing R machine MP: 100 W Y-shaped coater blade	Cubes (W×L×T) 9.2×18×3 mm³ 6.25×16×3 mm³
Nath et al. 2019 [91]	Mostly spherical	D10–17 D50–28 D90–47	20	90	---	600	120	Continuous line strategy with alternating layers at −45° and 45°	Atmosphere: argon Platform: mild steel VED: 63.0 J/mm³	Concept Laser Mlab cusing R machine Yb fibre laser MP: 100 W LBD: 50 µm Y-shaped rubber-coated blade	Cubes (10×10×10 mm³)
Krakhmalev et al. 2015 [94]	Spherical	D10–8 D50–23 D90–38	40	60	70	120	120	Rescanning strategy (each layer was scanned twice by the laser)	Atmosphere: nitrogen	Single-mode continuous-wave Yb fibre laser λ: 1075 nm MP: 200 W	Cubes (10×10×10 mm³)
Zhao et al. 2015 [53]	Spherical	20 (mean value)	20	100 110 120 130 140	80	400 500 600 700 800	80	---	Atmosphere: argon	HRPM-II-type SLM machine Continuous fibre laser MP: 200 W λ: 1064 nm	Cylinders (Ø10×40 mm³)
Yadroitsev et al. 2015 [50]	---	D10–8.2 D50–22.5 D90–37.6	50	50 to 70	70	80 to 160	120 140	Two-zone strategy	Atmosphere: nitrogen Platform: 304L stainless steel	Single-mode continuous-wave Yb fibre laser λ: 1075 nm MP: 200 W	Cubes (10×10×10 mm³)

BD build direction, *L* length, *MP* maximum power, *PSD* particle size distribution, *SLM* selective laser melting, *T* thickness, *VED* volumetric energy density, *W* width, *420SS* 420 stainless steel, *420SS+* 420 stainless steel with Nb and Mo, *λ* wavelength

*Parameters used to produce the final parts; **This study includes the analysis of properties with and without the addition of Nb (1.2 wt%) and Mo (0.57 wt%)

Table 2 Overview of the inputs of the LPBF process for the production of H13 steel parts

First author, year	Powder parameters		Laser parameters			Scan parameters			Other parameters	LPBF machine	Part's geometry/dimensions
	Particle shape	PSD (μm)	Layer thickness (μm)	Laser power (W)	Spot size (μm)	Scan speed (mm/s)	Scan spacing Hatch spacing (μm)	Scan pattern			
Narvan et al. 2021 [104]	Spherical	D10–28 D50–38 D90–52	40	150 200 250 300	100	400 600 800 1000	120	Continuous laser mode (stripe hatching pattern)	Atmosphere: N$_2$ Platform: 200 °C	EOS M280 machine Yb-fibre laser MP: 400 W	Cubes (10×10×10 mm)
Garcias et al. 2021 [113]	---	10–45	30	100	---	250–300	120	---	---	SLM 125 machine	---
Kunz et al. 2021 [105]	Spherical	D10–22.8 D50–32.6 D90–49.0	50	195	---	900	100	---	Atmosphere: argon Platform: 200 °C	Realizer SLM 100	Cubes (10×10×10 mm)
Katancik et al. 2020 [69]	Spherical	D10–26 D50–36 D90–50	50	152* 177 203 228	---	100* 500 800 1100 3000	40	---	Atmosphere: nitrogen (oxygen content below 0.1 vol.%)	ORLAS CREATOR SLM Yb fibre laser MP: 250 W Spiral recoater BC: Ø100×100 mm PLT: 20–100 μm Atmosphere: argon or nitrogen	Cylinders (Ø8×11.5 mm³)
Tomas et al. 2020 [74]	---	---	30	CT: 100 F: 150 CR: 175	70–80	CT: 400 F: 450 CR: 720	CT: 90 F: 80 CR: 120	2 strategies - Sectional - Stripe (incremental rotation of 33°)	Atmosphere: argon Platform: 200 °C Build direction** - 0°: in z-direction - 90°: parallel to z-direction	SLM 280HL metal printing machine YLR fibre laser MP: 400 W BC: 280×280×350 mm	Thin-walled rings (Ø85, 50 and 25, thickness 1, height 30 mm)
Yonehara et al. 2020 [106]	Spherical***	D10–19 D50–28 D90–42	1st mode: 50 2nd mode: 100	1st mode: 175–375 2nd mode: 600–1000	1st mode: 80 2nd mode: 300	1st mode: 400–1000 2nd mode: 100–260	1st mode: 100–140 2nd mode: 700	---	Atmosphere: nitrogen gas (oxygen content of less than 0.1%) Platform: 200 °C VED: 1st mode 54.2–114.6 J/mm³ VED: 2nd mode –34.4–142.9 J/mm³	SLM 280 HL Hull-core method - 1st mode: 400 W single-mode fibre laser (hull) - 2nd mode: 1000 W multi-mode fibre laser (core) BC: 280×280×350 mm MSS: 15 m/s PLT: 0.02–0.15 mm	Cubes (15×15×30 mm³)

Table 2 (continued)

First author, year	Powder parameters		Layer thickness (µm)	Laser parameters		Scan parameters			Other parameters	LPBF machine	Part's geometry/ dimensions
	Particle shape	PSD (µm)		Laser power (W)	Spot size (µm)	Scan speed (mm/s)	Scan spacing Hatch spacing (µm)	Scan pattern			
Pellizzari et al. 2020 [107]	Spherical	---	50	---	---	---	120	Alternate-hatching pattern	Atmosphere: argon (oxygen content lower than 0.6%) VED: 200.0 J/mm³ Build direction****: 0°, 45°, and 90°	MCP HEK REALIZER II Nd: YAG laser	---
Dzukey et al. 2020 [108]	Spherical	15–45	30	1st study 160 200 240 2nd study 160 190 220 260	70	1st study 400 800 1200 2nd study --	80	---	Atmosphere: (oxygen content below 0.1%) Platform: steel substrate (100×100×20 mm) VED (2nd study): 125.0, 148.4, 171.9, and 203.1 J/mm³	HRPM-II 3D printer Fibre laser λ: 1070 nm MP: 50 W BC: 150×150×150 mm PLT: 0.02–0.2 mm	Cubes (10×10×10 mm³)
Fonseca et al. 2020 [109]	Spherical with few satellite particles	D10–22 D50–33 D90–50	30	97–216	---	300–700	80	(Pattern rotation between layers–32°)	Atmosphere: argon Platform: 25 °C (no preheating)	AM OmniSint-160 machine Yb: YAG fibre laser MP: 400 W BVC: Ø156×200 mm	Cubes (10×10×10 mm³)
Pellizzari et al. 2020 [110]	Spherical	D10–19 D50–31 D90–51	50	100	---	249 167 56***	120	Alternate-hatching pattern	Atmosphere: argon (oxygen content below 0.6%vol.) VED: 67.0, 100.0, and 300.0 J/mm³	MCP HEK REALIZER II Nd: YAG laser	Rectangular (30×30×6.5 mm³)
Zhao et al. 2020 [111]	Spherical	---	20	160 180 200 220	---	750 1000 1250 1500	90	Reciprocating scanning strategy	Atmosphere: argon Platform: 45 steel VED: 88.9, 100.0, 111.1, 122.2, 148.2, 88.9, 74.1 J/mm³	EOS M280 Fibre laser λ: 1064 nm	Cubes (9×9×9 mm³)
Yan et al. 2020 [112]	Spherical	10–66 D50–27	30	175	64	725	100	---	Atmosphere: argon Platform: 200 °C	SLM 125 HL Ytterbium fibre laser λ: 1070 nm MP: 400 W (continuous wavelength mode)	Cubes (10×10×10 mm³)

Table 2 (continued)

First author, year	Powder parameters		Layer thickness (μm)	Laser parameters		Scan parameters		Scan pattern	Other parameters	LPBF machine	Part's geometry/ dimensions
	Particle shape	PSD (μm)		Laser power (W)	Spot size (μm)	Scan speed (mm/s)	Scan spacing Hatch spacing (μm)				
Džugan et al. 2020 [118]	---	---	---	175	---	610	---	Stripe hatch strategy (laser tracks were rotated 90° for each layer)	Atmosphere: nitrogen (oxygen content below 0.02 vol.%) Platform: 200 °C BD: XZY, 45°XY, ZXY	SLM280HL Yb: YAG laser MP: 400 W	Cylinders (∅25×20 mm³)
Wang et al. 2020 [95]	Spherical	D10–11 D50–27 D90–52	40	280	---	980	120	---	Atmosphere: argon Platform: 90–93 °C	---	Cubes (30×18×3.2 mm³)
Yan et al. 2019 [15]	---	Mean size≅25	30	175	70–100	725	100	(P1) bidirectional line route (no rotation) (P2) similar to (P1) (rotation of 90°) (P3) spirally scanned in the loop route	Atmosphere: argon Platform: 200 °C BD: longitudinal (L) and transverse (T)	SLM 125HL system BC: 125×125×125 mm IPG fibre laser λ: 1075 nm MP: 400 W (in continuous wavelength mode)	Cubes
Lee et al. 2019 [68]	---	---	25	90	---	(S2) 200 (S4) 400 (S8) 800	80	---	---	Concept laser M-LAB	Cubes
Narvan et al. 2019 [66]	Spherical	D10–28 D50–38 D90–52	40	(A) 100 (B) 200 (C) 300	---	200 400 600 800 1000 1200	80 120	Stripe scanning strategy (67° scanning rotation)	Atmosphere: nitrogen (oxygen content below 0.1%) Platform: 200 °C VED: 17.4–465.8 J/mm³	EOS M280 machine Fibre laser system MP: 400 W	Cubes (10×10×15 mm³)
Ren et al. 2019 [96]	Spherical***	15–50	40	1st study 160 170 180 2nd study 160	---	1st study 350 2nd study 350 400 450	100	---	Platform: 45# steel	EOS-M290 SLM machine Yb: YAG laser (fibre laser) MP: 400 W MSS: 7000 mm/s BC: 100×100×200 mm	Cubes (10×10×10 mm³)
Deirmina et al. 2019 [97]	Spherical	D10–19 D50–31 D90–51	50	100	---	249, 167, 56***	120	Alternate-hatching pattern (rotation of 90°)	Atmosphere: argon VED: 67.0, 100.0, 300.0 J/mm³	MCP HEK REALIZER II	Cylinders (∅ 4×10 mm³) Cubes (7×30×30 mm³)
Wang et al. 2019 [98]	Spherical	D10–10 D50–25 D90–49	40	280	---	980	120	Single pattern of parallel scan lines (rotation of 67°)	Atmosphere: nitrogen	EOS M280 SLM machine	Cubes (10×10×3 mm³)

Table 2 (continued)

First author, year	Powder parameters		Layer thickness (µm)	Laser parameters		Scan parameters			Other parameters	LPBF machine	Part's geometry/dimensions
	Particle shape	PSD (µm)		Laser power (W)	Spot size (µm)	Scan speed (mm/s)	Scan spacing / Hatch spacing (µm)	Scan pattern			
Åsberg et al. 2019 [114]	---	D10–19 D50–32 D90–51	30	Core 175 Contour 150	---	Core 720 Contour 450	Core 120 Contour –	Core-contour strategy; Contour–two borders and one fill contour; Core–stripe pattern	Atmosphere: argon Platform: 200 °C	SLM 125 HL system Fibre laser BC: 125×125×125 mm MP: 400 W	Cubes (20×20×60 mm³)
Jung et al. 2019 [99]	Spherical with a few satellites	D50–35	250	90	---	Dual scan speed combination 100–1000	800	---	Atmosphere: argon (oxygen content below 0.3) Platform: 316L stainless steel	M. LAB (Concept Laser Co)	Cubes (10×10×10 mm³)
Yan et al. 2019 [115]	---	D10–15 D50–27 D90–45	30	175	64	720	100	---	VED: 81.0 J/mm³	SLM 125 HL machine Ytterbium fibre laser λ: 1070 nm MP: 400 W Continuous wavelength mode	Cubes (10×10×10 mm³)
Nguyen et al. 2018 [119]	---	10–45	25	90	---	200–1600	80	---	Atmosphere: argon	Concept LaserMlab-Cusing system Nd: YAG fibre laser λ: 1064 nm	Cubes (10×10×10 mm³)
Deirmina et al. 2018 [100]	Spherical	D10–19 D50–31 D90–51	50	100***	---	167 250	120	Alternate-hatching pattern (90° rotation)	Atmosphere: argon VED: 100.0 and 67.0 J/mm³	MCP HEK REALIZER II	Cylinders (Ø 4×10 mm³)
Krell et al. 2018 [117]	---	25–63 D32–33	30	100	90	200–400 (best: 300)	100***	---	Atmosphere: argon (oxygen content below 0.3 vol.%) Platform: RT, 100, 200, 300 °C VED: 111.1 J/mm³	MCP HEK REALIZER II λ: 1076.5 nm MP: 100 W	Cubes (5×5×10 mm³)
Körperich and Merkel 2018 [116]	---	---	30	CT: 150 CR: 175 FL: 300	---	CT: 450 CR: 720 FL: 400	100	---	Platform: (Ø 90×100 mm) 650 °C	SLM 280 HL machine Yb fibre laser MP: 400 W	Cubes (10×10×90 mm³)
Ackermann et al. 2018 [101]	Spherical***	D10–24 D50–38 D90–59	30	CT: 100 CR: 350	---	CT: 470 CR: 1,400	CT: – CR: 120	(90° between successive layers)	Atmosphere: nitrogen (oxygen content 0.1%)	SLM 280 HL YLR fibre laser MP: 400 W	Tensile tests DIN 50,125 Charpy tests (55×10×10 mm³)

Table 2 (continued)

First author, year	Powder parameters		Layer thickness (µm)	Laser parameters		Scan parameters			Other parameters	LPBF machine	Part's geometry/ dimensions
	Particle shape	PSD (µm)		Laser power (W)	Spot size (µm)	Scan speed (mm/s)	Scan spacing Hatch spacing (µm)	Scan pattern			
Mazur et al. 2017 [57]	Spherical	D10–27 D50–38 D90–52	30	175	---	608	120	---	Platform: 200 °C VED: 80.0 J/mm³	SLM 250 HL	Cubes
Yan et al. 2017 [102]	Spherical	25–44	---	150	---	300	50	Alternate raster pattern	Atmosphere: argon Platform: 316L stainless steel (200 °C)	SLM 250 HL Yb: YAG laser MP: 400 W	Cubes (10×10×10 mm³)
AlMangour et al. 2016 [103]	Spherical	D10–24 D50–45 D90–142	50	100	180	250	120	Cross-hatching	Atmosphere: argon	---	Cylinders (∅ 8×6 mm³)

BC build chamber, *BVC* build volume capacity, *CHS* circular hollow section, *CR* core, *CT* contour, *F* fill, *FD* focal diameter, *FL* final layer, *MP* maximum power, *MSS* maximum scan speed, *PB* preheating system for the baseplate, *PSD* particle size distribution, *PLT* powder layer thickness, *RHS* rectangular hollow section, *RT* room temperature, *SHS* square hollow section, *SLM* selective laser melting, *VED* volumetric energy density

*Optimal processing parameters; **The angle describes the relative position on the substrate plate to the building direction; ***The parameter is estimated/calculated; ****Angle between the building direction and sample longitudinal axis

For the three steels, the highest density values (>99%) were obtained from high laser energy densities (high laser powers and low scanning speeds). The densification of LPBF parts occurs by diffusion in the liquid phase of the sintering process. Therefore, for the same material, the higher the energy transferred per unit of time is, the higher the energy density is, resulting in melt pools of suitable size, adequate re-melting of the previous layers, and good bonding between layers. This causes high densification and, consequently, lower porosity. For the higher cooling rates (higher scanning speeds), macro cracks resulting from thermal stresses have been detected (Fig. 5), leading to a lower final density of the parts [122–124]. The high temperature in the upper layers lead to their expansion. On the other hand, the underlying solidified layers have a lower temperature and restrict this expansion, inducing compressive stresses in the upper layers. When the yield strength is reached, the compressive stresses cause plastic deformation. On the other hand, when these layers cool, their compressive state is converted into residual tensile stresses that can lead to cracks [66].

For 420 stainless steel, a maximum densification of 99.95% was obtained for a laser energy density of 53.0 J/mm³ [53]. Nath et al. [86] revealed that for low energy densities (29.0 J/mm³), the use of a finer powder is beneficial in terms of densification, but this effect is attenuated as the energy density is increased by up to 63 J/mm³. An increase in the hatch spacing and laser spot size contributed to a decrease in densification [84, 89]. The width of the melt pool increases with an increase in laser spot size, whilst the depth of the melt pool slightly decreases with an increase in the size of the laser spot, leading to the formation of pores between the melt pool boundaries and at the edge between two layers. The melt pool depth may be less than the layer thickness defined, so there will be no complete layer densification [84]. Shen et al. [87] built the same component in three different directions, thickness direction (*t*), width direction (*w*), and length direction (*l*) with $t < w < l$. The component built in the thickness direction leads to higher densification, because the total number of layers to build the final component is smaller and, consequently, the porosity between successive layers associated with deposition of the new layers is lower.

Concerning H13 steel, the highest density reported in the literature is 99.70% and corresponds to a laser energy density of 60.0 J/mm³ [66]. The density of H13 steel can be enhanced by laser re-melting (dual scan) as mentioned in [99]. However, although the second scanning closes the pores on the top of the molten pool, the internal pores cannot be removed [7, 99, 101]. Thermo-mechanical treatments, particularly hot isostatic pressing (HIP) have been applied to improve the density of the LPBFed H13 steel parts [7, 114, 125, 126]. By increasing the temperature and pressure, HIP allows diffusion between the chemical elements with

Table 3 Overview of the inputs of the LPBF process and properties of P20 steel

First author, year	Powder parameters		Laser parameters			Scan parameters			Other parameters	LPBF machine	Part's geometry/ dimensions
	Particle shape	*PSD* (µm)	*Layer thickness* (µm)	*Laser power* (W)	*Spot size* (µm)	*Scan speed* (mm/s)	*Scan spacing Hatch spacing* (µm)	*Scan pattern*			
Yan et al. 2019 [115]	---	D10–18 D50–29 D90–46	30	200	64	800	105	---	VED: 79.4 J/mm^3	SLM 125 HL machine Ytterbium fibre laser λ: 1070 nm MP: 400 W Continuous wavelength mode	Cubes (10×10×10 mm^3)
Lin et al. 2019 [120]	Spherical	Mean size–25	30	150	60	800	80	Zig-zag (67° rotation)	Atmosphere: argon	HBD-100D SLM machine Fibre laser	Cubes (10×10×4 mm^3)
Li et al. 2018 [121]	Spherica*	D10–48 D50–70 D90–101	30	100 120 140 160	---	150 250 300 350 400	80	---	Atmosphere: argon Platform: 316L stainless steel VED: 138.9– 333.1 J/mm^3	DiMetal-100 Yb: YAG laser MP: 400 W	Cubes (10×10×10 mm^3)

MP maximum power, *PSD* particle size distribution, *SLM* selective laser melting, *VED* volumetric energy density, *λ* wavelength

*The parameter is estimated/calculated
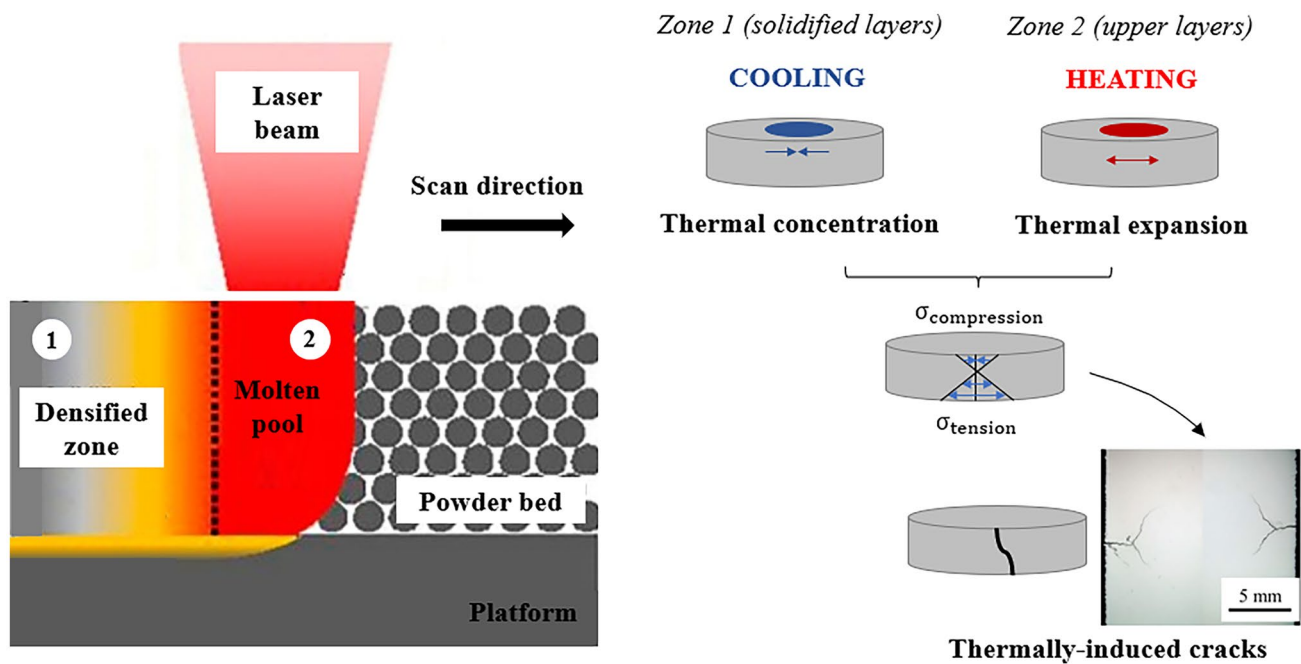
Fig. 5 Thermal stresses in LPBF process and origin of thermally induced cracks (based on [7, 66])

consequent reduction of porosity and formation of more homogeneous microstructures [7, 113, 127]. Wang et al. [7] demonstrated that the relative density was increased from 80.50 to 98.20% by HIP treatment.

For P20 steel, the maximum density reached was 99.50%, for a density energy value of 79.4 J/mm^3 [115]. As for the previous materials, increasing laser power and decreasing scanning speed are beneficial for this property [121].

4.2 Microstructural properties

The microstructural properties of the LPBFed parts, such as morphology, segregation, grain structure (shape and size), stability, secondary phases, defects, and inclusions, depend on the processing parameters [1]. The thermal history to

which the metal is exposed during the LPBF process is very different from that of traditional manufacturing processes [1, 7]. LPBF induces rapid solidification rates and high thermal gradients caused by the melting of the various subsequent layers [1, 128, 129]. The high cooling rate gives rise to high nucleation rates and the consequent microstructure refinement [4, 7, 130].

The microstructure of LPBFed 420 stainless steel parts is mainly composed of fine martensitic needles/laths, and some residual austenite (cellular structures) (Fig. 6) [85, 89–94, 131].

No carbides are reported in the literature in LPBFed parts of this steel, which can be explained by the low carbon content (< 0.15 wt% C) and high cooling rates that minimises the diffusion mechanism and thus prevents the formation

Fig. 6 Typical microstructure of 420 stainless steel produced by LPBF (after polishing followed by etching with Kalling reagent II) (adapted from [91, 131])
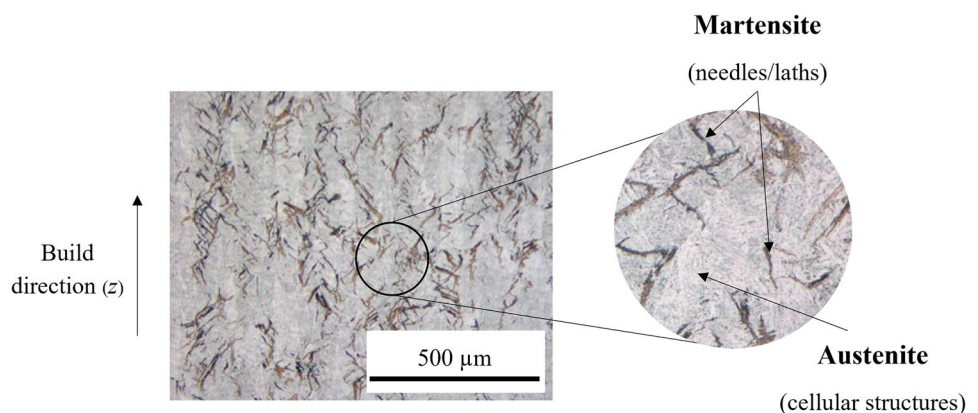
of equilibrium structures [89, 132]. Striking differences are observed in the orientation of the martensite needles in the build and scan directions. An increased directionally is observed in the scan direction, with the needles located at the edge of the scan tracks due to the faster cooling rates near the edge of the melt pool [91]. Nath et al. [89] showed that the martensite content in the microstructure of LPBFed 420 stainless steel parts increased when the layer's thickness decreased. This can be explained by the fact that they experience a higher number of thermal cycles. The addition of alloying elements, namely Nb and Mo, did not reveal significant changes in the contents of martensite and residual austenite [93]. However, some nanoscale transition metal carbides (NbC) are formed during processing, which, as will be discussed below, play a key role in improving the mechanical properties [92, 93]. Laser power also influences the microstructure of 420 stainless steel. Zhao et al. [53] found that the amount of the martensite phase decreases with an increase in this parameter, due to the higher temperature of the molten pool, and lower cooling rate, with a consequent higher amount of residual austenite. The higher the temperature reached in the part during the process is, the greater the dissolution of the chromium carbides existing in the base material and the incorporation of carbon and chromium in the austenitic phase are. This lowers the starting temperature of the martensitic transformation with a consequent decrease in the percentage of this phase in the final microstructure. On the contrary, when the laser power decreases, the cooling rate increases, and a higher amount of martensite is formed. Nath et al. [86] claim that LPBFed parts processed at the same energy density using fine and coarse powders show no significant difference in the microstructure. After post-processing operations, some differences may be verified in the microstructure [85, 88, 89, 91, 93]. Tian et al. [85] and Shi et al. [88] state that the as-built parts are formed by martensite and retained austenite with strong mechanical property anisotropy in both strength and ductility. In these studies, a fully tempered martensitic microstructure with some dispersed $Cr_{23}C_6$ carbides was obtained after tempering. Other authors also mention the removal of residual stresses during this heat treatment [89, 91, 93].

Concerning H13 steel, the LPBFed microstructure of the parts includes martensite and large amounts of austenite [7, 100]. During solidification, the high cooling rate involves a lower diffusion of the alloying elements Cr, Mo, and V, and, therefore, no formation of carbides occurs [7, 133]. The rapid solidification inherent to the process leads to the segregation of alloying elements at the boundary of the molten pool and results in a cellular/dendritic microstructure [7, 95, 97, 100, 107, 112]. Since carbon, chromium, and vanadium are austenite stabilisers, the amount of this phase after cooling is higher in the regions with a higher concentration

of carbon atoms [7]. The grain size of austenite is of a few microns (about 1–5 μm) [7, 68, 97, 98, 106, 112, 117]. Three distinct types of grain structures are highlighted in [7, 15], depending on the temperature gradients and, the consequent growth rates during solidification: (i) columnar, (ii) fine cellular, and (iii) coarse cellular (Fig. 7).

The microstructure in the centre of the molten pool is relatively coarse due to the high temperatures and cooling times [7, 135]. On the other hand, the microstructure of the cross-section along the building direction consists of columnar grains going in this direction. This can be explained by the heat conduction that makes the grain elongate along direction of the laser scanning [68, 103, 127]. The energy density also affects the grain structure. Similar to 420 stainless steel, the higher the energy density (higher temperature at the surface of the part under construction) is, the lower the tendency for the formation of columnar grains is [7, 136], and the higher the amount of residual austenite and its grain size is too [97, 108]. The preheating of the base plate during the LPBF process is another factor that plays an important role concerning the microstructure [104]. It results in lower cooling rates, and consequently higher amounts of retained austenite [66, 117]. Contrarily to the energy density, an increase in the scanning speed leads to a decrease in the grain size [68]. The higher the scanning speed is, the lower the surface temperature, the diffusivity, and the grain size are.

In order to decrease the amount of residual austenite and to improve the toughness of the LPBFed parts, quenching and tempering heat treatments are performed [69, 95, 97, 102, 107, 110, 112, 114, 117]. During quenching, the austenite in the cellular grain boundaries (austenite indicated by the arrows in Fig. 8a) is eliminated and a full martensite microstructure is formed (Fig. 8b) [7, 66, 97, 98, 107, 110]. During tempering, martensite loses carbon as the temperature increases and carbides are formed, initially of iron and later of stronger carbide forming elements [7, 69, 97, 107, 110, 112, 117]. The typical tempered microstructure is composed of tempered martensite, ferrite, and secondary carbides (Cr, Mo, and V carbides) [7, 69, 97, 98, 105, 107, 112, 117] (Fig. 8c).

Regarding P20 steel, the information available in the literature is scarce. Li et al. [121] reveal that the microstructure of LPBFed P20 steel parts consists of martensite laths and some residual austenite dendrites. As expected, a finer grain structure was observed in the middle of the melt pool (higher energy intensity), and coarse grains were detected in the most peripherical zone of the melt pool (heat affected zone in the weld) [120, 121]. After tempering, the martensite phase is progressively transformed into tempered martensite and fine carbides precipitated between the martensite laths [121].
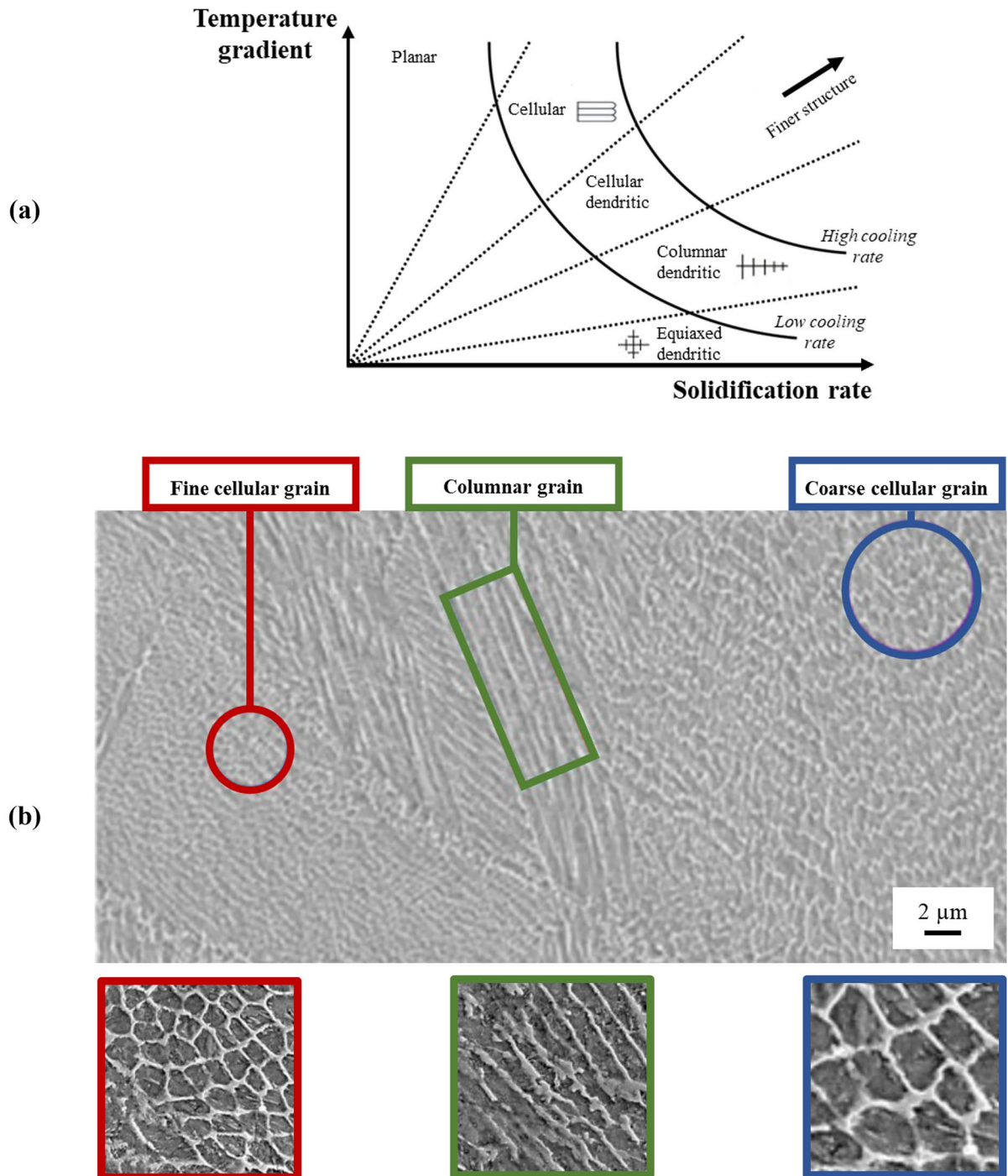
Fig. 7 Solidification structures: **a** the effect of temperature gradient and solidification rate on the grain, and **b** H13 LPBFed samples morphology (adapted from [7, 134])
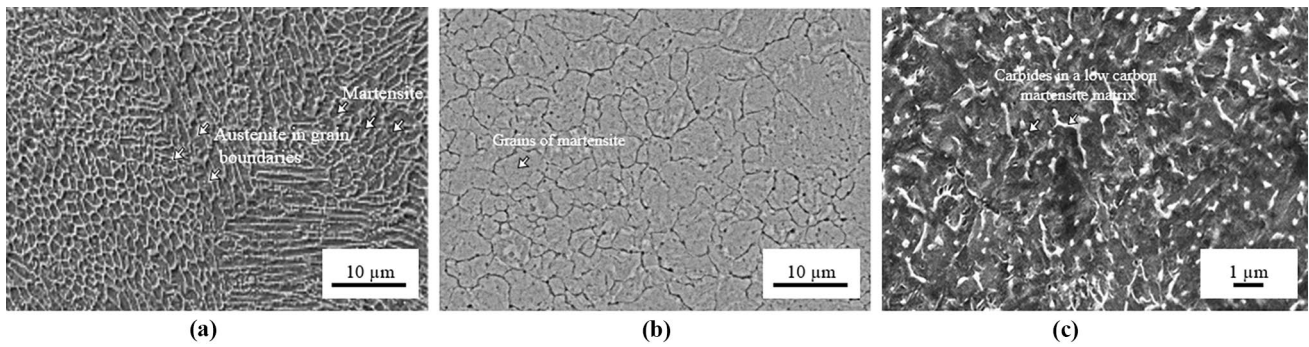
Fig. 8 Microstructure of H13 steel produced by LPBF: **a** as-built condition, **b** after quenching, and **c** after tempering (adapted from [7, 98])

4.3 Quality of surface finish

Surface roughness is one of the most important features of components fabricated by LPBF, namely for the plastic injection moulding industry as it directly influences the appearance of the final product [5, 7]. There are two main causes of surface roughness associated with the AM processes, the *staircase effect*, and the insufficient melting of the powder particles/balling effect [5, 7, 137, 138]. The first is related to the stepped approximation of layers of curves and inclined surfaces, and depends on the layer's thickness (t) and build angle (θ) [5, 139], according to Eq. (2).

$$R_a = 1000t \times \sin\left(\frac{90 - \theta}{4}\right)\tan(90 - \theta) \qquad (2)$$

where R_a is the arithmetic mean of the surface roughness, t is the layer's thickness, and θ is the build angle. The *staircase effect*, and consequently the surface roughness, can be reduced by decreasing the layer thickness or by increasing the build angle [5, 140]. For lower layer thickness, a low scanning speed and a long dwell time are needed to melt the thicker powder layer fully. This causes process instability, which leads to balling and splashing during the scanning process and a high final roughness (Fig. 9). Concerning the build angle, Leary [141] states that for low values ($\theta \rightarrow 0°$), staircase effects dominate, and the roughness observed is high. As the orientation of the surface increases, the staircase effects coalesce, and roughness is predominantly the result of the presence of adhered, partially melted particles. However, for orientation angles higher than 75°, the roughness does not improve any further, because this effect does
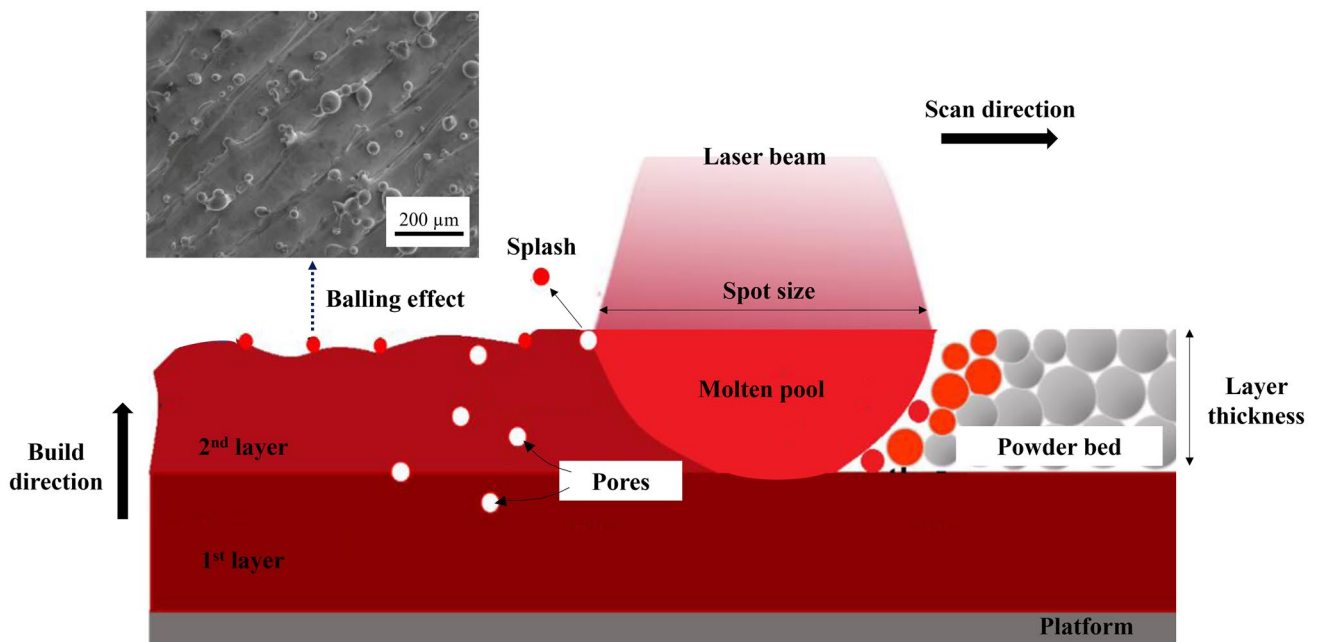
Fig. 9 Interaction between laser and powder bed: balling effect phenomenon (adapted from [7, 19, 66])

not play a role anymore and other effects, such as balling, cause the roughness to increase [140].

The second mechanism is related to energy density, particularly laser power and scanning speed [5, 7, 137, 138]. High laser power can lead to evaporation and splashing in the molten metal pool [7], whilst a low laser power causes a balling effect, because the sintering temperature decreases, leading to an incomplete melting of the powder particles and a reduction in the amount of liquid [7, 142] (Fig. 9). The balling effect occurs when the molten material does not wet the underlying substrate due to the surface tension leading to the formation of individual spherical drops instead of merging the fusion pools along the scan tracks. Therefore, there is an undesired formation of single melt drops instead of a continuous melt pool. This fact results in a rough and not uniform surface, impeding a smooth layer deposition and decreasing the densification of the final part [7, 138].

Concerning scanning speed, high values allow the melted drop to be splashed easily [5, 7]. Wang et al. [7] claim that in this case, the molten sintering track is highly unstable and the surface energy of the liquid trajectory will continually decrease to obtain the final equilibrium state, leading to the abovementioned phenomenon. Increasing the scanning speed leads to a decrease in the energy density and, consequently, to a decrease in the working temperature and melting path diameter (same as the melt pool width, corresponding to the maximum size affected by a single track of the laser scanning) [7, 143]. Contrarily, for slow scanning speeds, the interaction time between laser and powder increases, which leads to a large molten pool. This results in a lack of powder in the original position, and a low density and a high number of pores are obtained [5, 7, 143].

As expected from Eq. (2) and discussed by Nath et al. [89] for the particular case of 420 stainless steel, the surface roughness of the parts increased with the increasing thickness of the layer (Fig. 10).

The addition of alloying elements (1.2 wt% Nb and 0.57 wt% Mo) does not show any influence on the surface roughness for the same processing parameters [93]. Furthermore, Yang et al. [84] showed that the surface roughness along the laser scanning direction increases with an increasing laser spot size (Fig. 11).

This phenomenon can be attributed to the balling effect (verified to laser spot sizes of 30 and 40 μm (Fig. 11c, d), caused by a lower volumetric energy density. When the laser's energy density is too low to fully melt the powder, the wetting effect deteriorates, and the balling effect occurs due to the creation of large balls of adhered powder to the track. The powder size also has a significant influence on the surface roughness of parts produced by LPBF. For the same energy density, a finer powder leads to better surface finish [86]. Furthermore, Nath et al. [86] showed that the difference in surface roughness between a finer and coarse powder is minimal at a processing parameter of 63 J/mm³.

4.4 Mechanical properties

The mechanical properties are the key aspect for plastic injection moulds since during the injection cycle, the mould is subjected to cyclic mechanical stresses, due to the pressure inherent to the process. Moreover, the mechanical resistance prevents the deformation of the injected materials and, consequently, avoids defects in the final parts. They depend on the densification, microstructure, and chemical composition of the material of the mould.

Figure 12 shows the influence of the energy density and heat treatment on the hardness, yield strength, ultimate tensile strength, and elongation of 420 stainless steel parts produced by LPBF. Two main conclusions can be drawn from this figure: (i) there is no direct and clear relationship between the energy density and the values of the mechanical properties, although there is a certain tendency for property values to increase with an increasing energy density value and (ii) the heat treatments have different effects on the mechanical properties of the LPBFed parts. Concerning the as-built parts, the highest values of hardness, yield strength, ultimate tensile strength reported were obtained from a part

Ra = 3.0 ± 0.2 μm   Ra = 4.6 ± 0.4 μm   Ra = 13.6 ± 1.2 μm

(a)   **(b)**   **(c)**
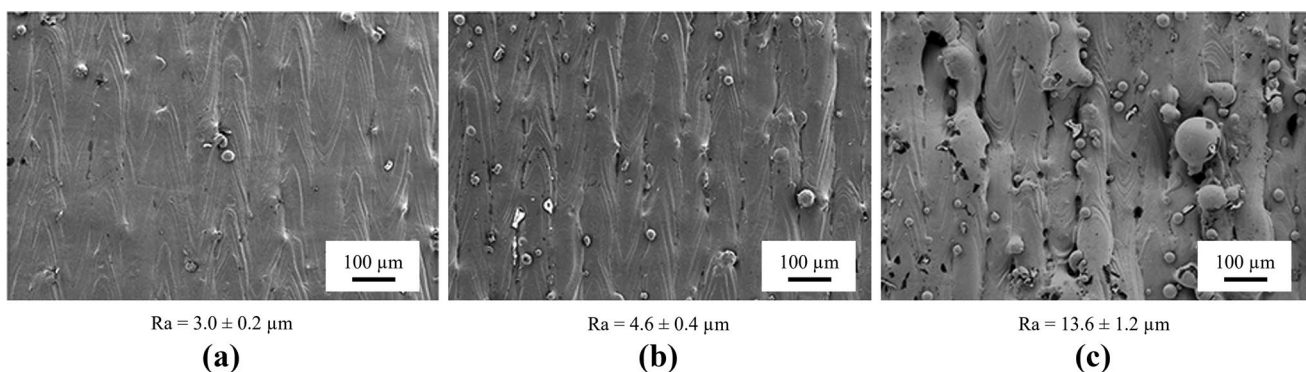
Fig. 10 Surface roughness of 420 stainless steel samples fabricated with different layer thicknesses: **a** 10, **b** 20, and **c** 30 μm (adapted from [89])
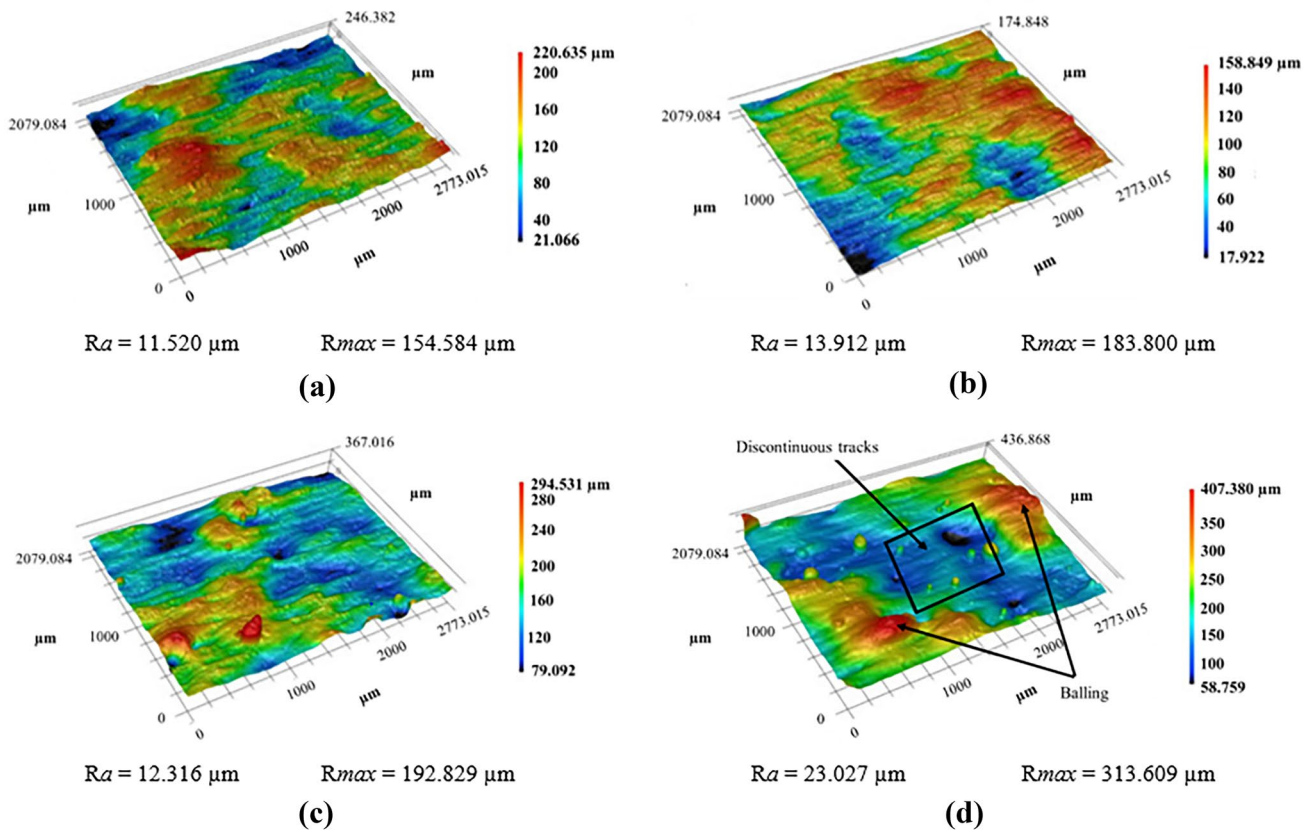
Fig. 11 Representative 3D profile of the top surface of samples produced with different laser spot sizes: **a** 10 μm, **b** 20 μm, **c** 30 μm, and **d** 40 μm (surface roughness along the laser scanning direction) (adapted from [84])

built with an energy density of 63.0 J/mm^3 and a final density of 99.30% [93]. As mentioned before, the highest density achieved in LPBFed parts from this steel was 99.95% for a laser energy density of 53.0 J/mm^3 [53]. However, as is known, the mechanical behaviour of the LPBFed parts is not just influenced by density, but also by the metallurgical and microstructural properties [5].

The ductility of 420 stainless steel can be improved by subsequent tempering, which changes the microstructure and reduces the residual stresses [91, 144]. According to the literature, tempering at temperatures lower than 425 °C is responsible for an increase in ductility without a considerable drop in the values of the other mechanical properties. This is due to: the decrease of residual stresses, the tempering of the martensite, and the formation of fine Cr-rich and Nb-rich carbides dispersed in the matrix [89, 91, 93]. A slight decrease in hardness and an increase in yield strength, ultimate tensile strength, and elongation are reported in many studies. According to Nath et al. [91], the decrease in the residual stresses together with the carbon loss from martensite may explain the decrease in hardness during tempering.

The addition of Nb (1.2 wt%) and Mo (0.57 wt%) in low-carbon steel alloys has been reported to improve the mechanical properties. However, it does not have an appreciable influence on the hardness of both as-built and heat-treated samples [93]. This result may appear surprising since these elements are strong carbide formers and both NbC and Mo_2C carbides are harder than the martensite microstructure with < 0.15 wt% C. However, their formation involves a decrease in the carbon in the martensite structure with a subsequent decrease in hardness.

Yang et al. [84] reported that, in general, a decrease in spot size (keeping the other processing parameters constant) leads to an increase in the tensile properties. When the spot size decreases (higher energy density), the re-heated zone decreases, and a higher temperature gradient is verified, allowing the formation of a finer microstructure. On the other hand, Nath et al. [86] revealed that the initial powder size does not have a significant effect on the mechanical properties of 420 stainless steel parts. However, the build direction influences the mechanical properties of LPBF components. Shen et al. [87] state that the yield strength and ultimate tensile strength are higher when the part is built in
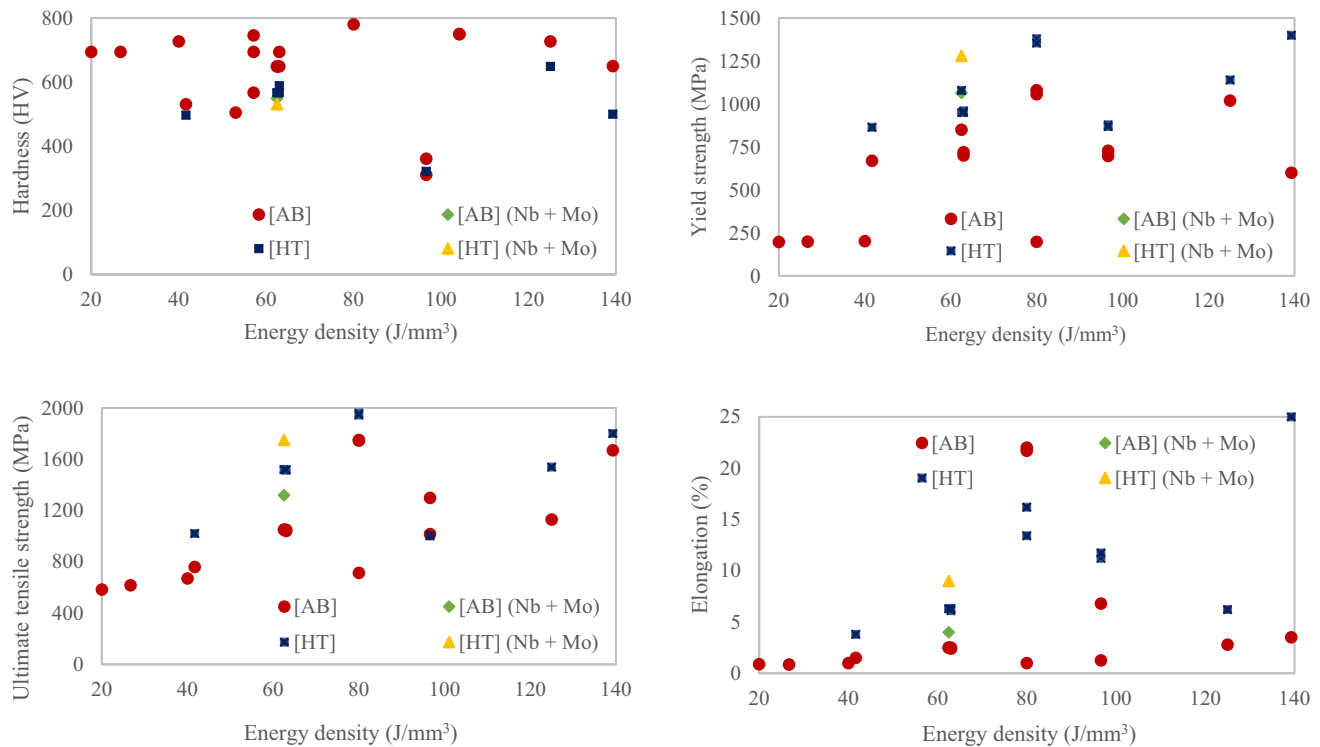
Fig. 12 The influence of the heat treatment on the hardness, yield strength, ultimate tensile strength, and elongation of 420 stainless steel parts (with and without Nb and Mo elements) produced by LPBF (AB = as-built, HT = heat-treated) [50, 53, 88–91, 93]

the direction of the higher dimension. On the other hand, the elongation increases inversely due to the variation of the densification.

It is important to compare the different values of the mechanical properties of the parts produced by LPBF (with and without posterior heat treatments) and other manufacturing techniques (Table 4). Although the mechanical strength of the LPBFed parts is superior to that of wrought and heat-treated or annealed cold drawn 420 stainless steel, the elongation tends to be lower [87, 90]. Once again, this is due to the higher cooling rates achieved by the LPBF

process, with the formation of a high martensite contents. Heat treatment mitigates these differences. The fracture surface of as-built parts is characterised by a fragile fracture mode typical of brittle components, whereas after the heat treatment the parts clearly showed a mixed-mode of fracture, consisting of ductile-fragile behaviour, which is responsible for the increase in elongation [84, 87, 90]. Comparing mechanical properties of the as-built LPBF, and MIMed parts, one can conclude that higher values are obtained by using the former process. In LPBF, the samples experience a large number of thermal cycles and have potentially different

Table 4 Mechanical properties of 420 stainless steel produced by different manufacturing processes (*MIM* metal injection moulding)

| Condition	Hardness (HV)	Yield strength (MPa)	Ultimate tensile strength (MPa)	Elongation (%)
LPBF [91]	649	700	1050	2.5
LPBF (tempered) [91]	567	950	1520	6.3
(Nb + Mo) LPBF [93]	549	1065	1320	4.0
(Nb + Mo) LPBF (tempered) [93]	531	1280	1750	9.0
Wrought (annealed) [1, 145]	---	626	800	6.0
Wrought (quenched and tempered) [85, 91]	567	1250	1625	7.0
MIM [91]	490	---	775	1.2
MIM (tempered) [91]	497	1100	1350	2.0
Annealed cold drawn [90, 146]	---	700	800	6.0–7.0

microstructures compared to other powder net-shaping processes such as MIM [61, 85, 93]. The improvement in yield strength, ultimate tensile strength, and hardness is mainly attributed to the grain refinement in the LPBFed parts. On the other hand, 420 stainless steel with the addition of Nb and Mo present the best properties due to the combination of the nanoscale NbC precipitation with the appearance of tempered martensite [93].

After a heat treatment (tempering) of both parts, the difference between the values is attenuated. Tempering leads to the transformation of retained austenite and martensite into ferrite and alloyed carbide precipitation, which induces an increase in both strength and elongation after heat treatment [85, 93, 147]. The influence of the energy density and heat treatment on the hardness, yield strength, ultimate tensile strength, and elongation of H13 steel parts produced by LPBF is presented in Fig. 13.

As for 420 stainless steel, no direct relationship exists between the energy density and the values of the mechanical properties. However, some authors claim that an increase in the energy density has a positive effect on the mechanical properties up to a certain value, particularly on hardness [97, 100, 108, 110].

Pellizzari et al. [110] claim that there is an optimum value of the energy density up to which the hardness increases and then lowers due to the increase in the fraction of retained austenite. The existence of a large amount of martensite, as well as the residual stresses associated with the high solidification rate inherent to the process, is beneficial to enhance the hardness [7, 127]. The hardness of H13 steel is strongly affected by the strain rate [7, 119]. Nguyen et al. [119] claimed that the hardness (indentation stress) of the LPBF-processed H13 material is susceptible to the strain rate. The hardness increased from 8.41 to 9.18 GPa for strain rates from 0.002 to 0.1 s^{-1} at a scanning speed of 100 mm/s. The effective stress of LPBF H13 has an approximately linear relationship with the logarithmic strain rate, implying an increase in hardness as the strain rate increases. The same hardness behaviour was observed for increasing scanning speeds. The values increased 9.2, 7.9, 11.5, 11.8, and 13.6% with increasing strain rate (0.002 to 0.1 s^{-1}), for scanning speeds of 100, 200, 400, 800, and 1600 mm/s, respectively. Based on the results, the authors claimed that the hardness of the H13 steel prepared by LPBF is less susceptible to the strain rate as the laser scan speed is reduced below 200 mm/s, but is more critically affected for values higher than 200 mm/s. Lee et al. [68] also reported that hardness increases for lower scanning speeds. The build direction is another aspect that influences the mechanical properties of the LPBFed parts made from H13 steel. Tomas et al. [74] and Džugan et al. [118] showed that the yield strength is higher when the part is built in z direction and decreases when the build direction is 90° to this axis. On the other hand, the elongation is higher when the build direction is
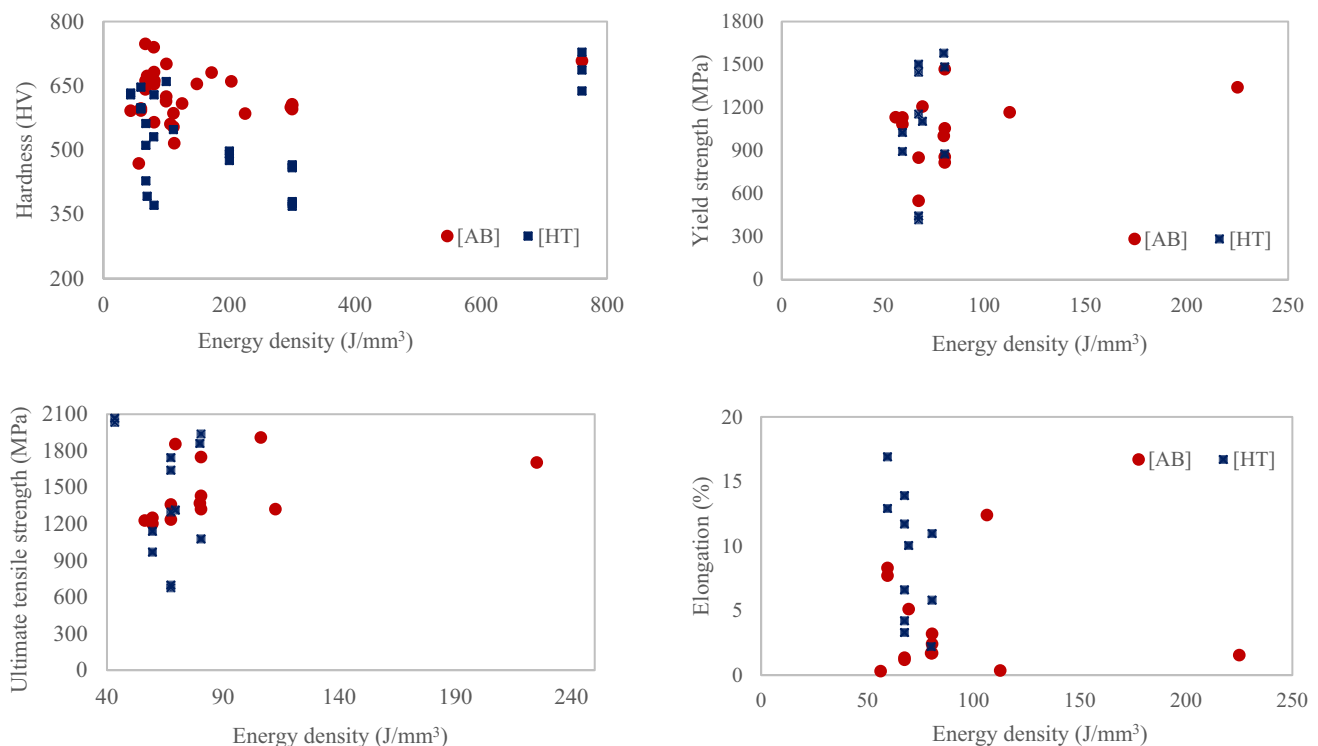
Fig. 13 The influence of the heat treatment on the hardness, yield strength, ultimate tensile strength, and elongation of H13 steel parts produced by LPBF (AB = as-built, HT = heat-treated) [15, 57, 68, 69, 74, 95–98, 100–102, 107–110, 112–114, 116–118]

90° to the *z*-axis. Džugan et al. [118] showed that the lowest ductility is related to the high concentration of defects, namely the lack of fusion defects and pores because they act as stress concentration sites.

As in the case of 420 stainless steel, the improvement of the mechanical properties of the H13 steel is usually achieved by heat treatments [57, 69, 98, 112, 114]. Higher values of mechanical properties were observed in many studies after tempering at around 525 °C (the temperature of the secondary hardening), ascribed to the decrease in the retained austenite content and the formation of secondary hardening phases (mainly V-enriched carbides) [69, 98, 105, 112]. The values of the mechanical properties of the LPB-Fed H13 parts after heat treatment are higher than those fabricated by conventional methods [98, 101, 112]. When compared to wrought H13 samples, LPBF parts maintain higher microhardness values during temperature treatments [69], probably because of a higher dislocation density, the refinement of the grain because of the rapid solidification, and a higher volume fraction of the formation of carbide nanoparticles.

For P20 steel, Li et al. [121] pointed out three different aspects that can contribute to the increase in the hardness of LPBFed parts compared to conventional processes: (i) the lower grain size, (ii) the existence of carbides in the microstructure, and (iii) the formation of a large amount of acicular martensitic structures. The hardness after heat treatment (tempering) decreases compared to the as-built condition for the same reason provided for the previous materials.

Another important mechanical property is fatigue strength, associated with the failure of metal components under cyclic loading, present in many applications, namely plastic injection moulds. Therefore, a component's fatigue performance is one of the most important factors in the LPBF process. Process-inherent properties, such as surface roughness and defects (i.e., size, shape, and the distance from surface), strongly influence the fatigue performance of LPBFed parts [1, 3, 107]. However, only a very few papers are available in the literature for these steels and those existing are only related to H13 steel. Some authors claim that a considerable improvement in fatigue life can be achieved by surface machining to remove the surface defects of the LPBF parts [1, 148, 149]. Different reasons have been presented to explain the inferior fatigue behaviour of LPBFed H13 steel parts compared to conventional methods [1, 57, 107, 113, 150]. The main reasons are the high surface roughness, and residual stresses, which promote crack initiation [1, 57, 105, 107, 118]. However, with a stress-relieving treatment, the fatigue life of LPBFed parts may increase significantly [57, 107]. The other challenge to this technology is inhomogeneity throughout the part [1]. A non-uniform tempering, due to the heat transfer from the solidifying layer to the previous layers, is responsible for a heterogeneous distribution of properties [1, 97].

Pellizzari et al. [107] studied the effect of building direction (0, 45, and 90° to the *z*-axis) and defect sensitivity on the fatigue behaviour of additively manufactured H13 tool steel. The authors concluded that the fatigue strength for 0° is lower than that for 45° and especially 90°, due to the difference in residual stresses and the orientation of the defects concerning the load applied. Samples built in the z-direction (0°) are characterised by a lack of fusion defects with a split shape perpendicular to the loading axis, which leads to a higher stress concentration factor compared the 90° samples. The size of the defect is smaller for the samples with a 90° orientation.
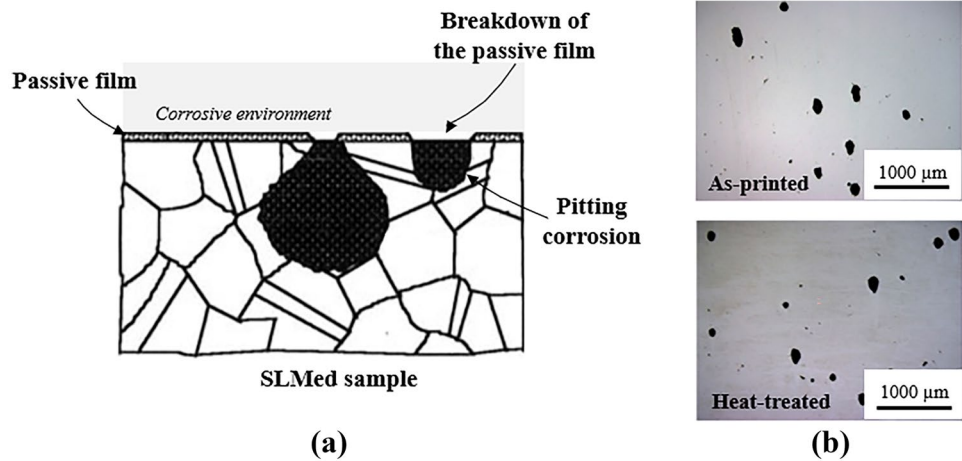
4.5 Corrosion properties

The corrosion properties of plastic injection moulds are very important due to the corrosion caused by the plastic material and any eventual additives at elevated temperatures [33, 52]. They depend on the microstructure, porosity, and chemical composition of the material of the mould [1, 89]. Moreover, lack of fusion pores is referred to as being more detrimental to corrosion properties than spherical pores, since they act as pit formation sites in a corrosive environment [1, 151, 152] (Fig. 14a).

There are some studies on the corrosion behaviour of LPBFed parts built from 420 stainless steel and P20 steel. The corrosion resistance of 420 stainless steel is associated with the presence of chromium, which enables the formation of a chromium oxide passive film on the metal surface [89, 91, 93, 153]. The corrosion resistance of LPB-Fed 420 stainless steel parts has been the subject of different studies, in particular with regard to particle size, layer thickness, the addition of alloying elements, and heat treatments [86, 89, 91, 93]. A summary comparison of the influence of these factors on the corrosion properties is given in Table 5.

The initial powder size has a significant effect on the corrosion properties of 420 stainless steel parts. Fine powder increases the corrosion properties of the final parts, since for the same processing parameters, high densification is obtained [86]. Nath et al. [89] claim that the higher corrosion resistance observed for samples fabricated at lower layer thicknesses is due to the high densification and higher amount of martensite. On the contrary, pitting corrosion occurred for higher layer thicknesses. The addition of alloying elements, such as Nb and Mo, is beneficial for corrosion properties, because both elements act as stabilising agents, reducing the tendency to undergo intergranular corrosion [93]. The heat treatment does not have a significant effect on the corrosion properties of

Fig. 14 Corrosion: **a** schematic representation of pitting corrosion (adapted from [155]) and **b** pits on 420 stainless steel surface produced by LPBF on the as-printed and heat-treated conditions (adapted from [91])

LPBFed 420 stainless steel parts [89, 91, 93] (Fig. 14b). Comparing the corrosion properties of the as-built LPBF and wrought parts, one can conclude that lower properties are obtained by using the former process. The formation of non-equilibrium microstructures during LPBF process and the final porosity are regarded as the main reasons for the reduced corrosion resistance [154].

For P20 steel, and contrarily to 420 stainless steel, the as-built LPBFed parts showed poorer corrosion resistance than the heat-treated ones and as-supplied samples, which might be explained by the inherent porosity that originates crack corrosion and the formation of martensite [121]. The tempering of martensite and the resulting relief of the residual stresses leads to increased corrosion properties [121].

4.6 Tribological properties

The tribological properties, particularly wear resistance, are crucial for plastic injection moulds to guarantee efficacy and safety [156], especially when the injected material is reinforced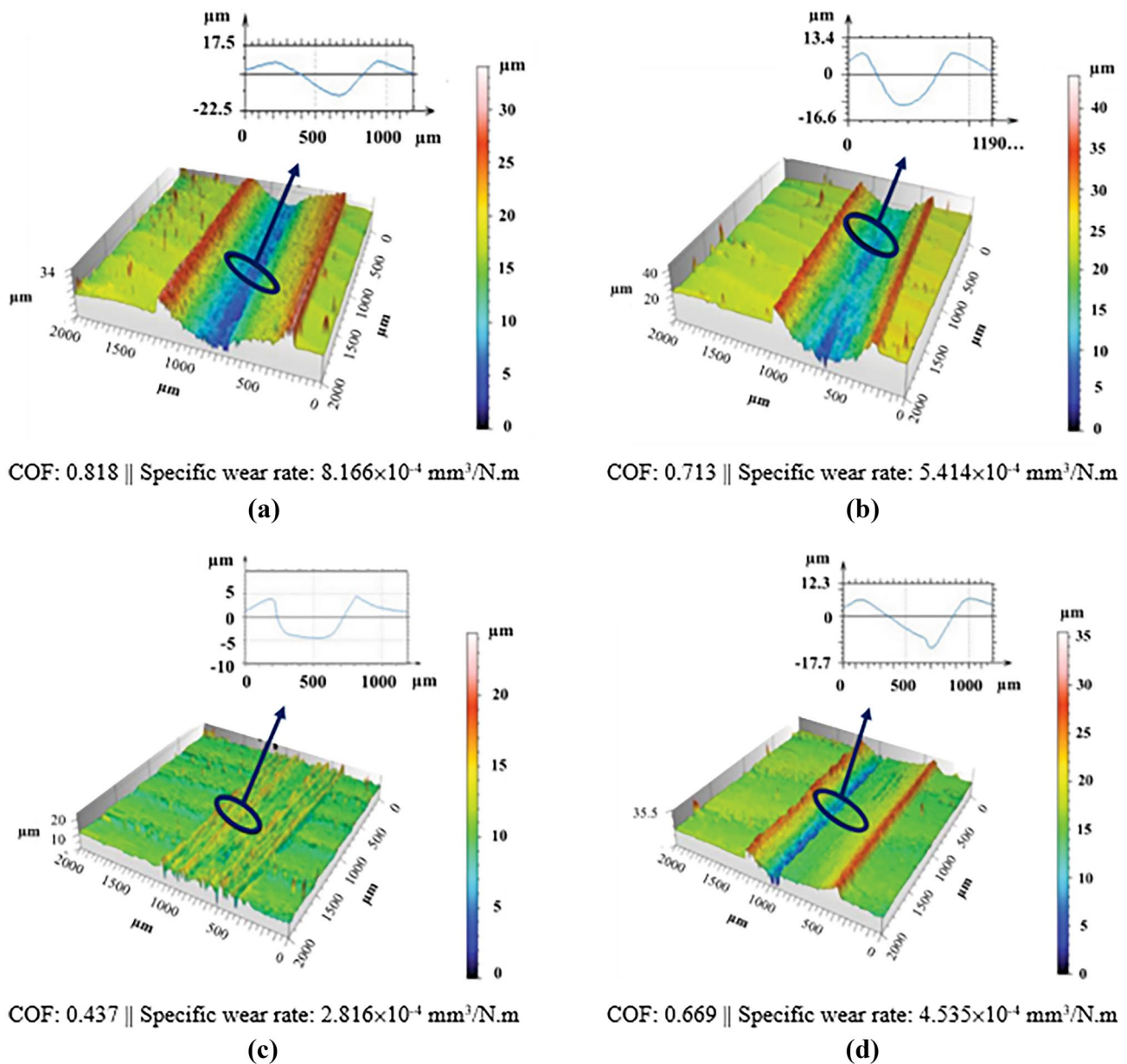 with hard particles, such as glass fibre reinforcements, or when additives like titanium oxide are used [31, 52]. The tribological properties are dependent on the microstructure (type of phase(s), shape, and size), porosity, and surface roughness [157]. Some studies show that the wear resistance of materials processed by LPBF improves when compared to traditional manufacturing processes due to the refined microstructure achieved by the process [156–158].

Tribological results can be found in the literature for LPBFed parts made of H13 and P20 steels. Dzukey et al. [108] performed wear sliding tests of LPBFed parts of H13 steel against 6-mm-diameter ceramic balls, at 20 N loading, with a speed of 100 r/min for 60 min (room temperature and dry friction). The author showed that the tribological behaviour of LPBFed parts of H13 steel depends on the energy density. The surface morphology of the wear tracks for samples produced with different energy densities is shown in Fig. 15.

When the energy density increases, the specific wear rate and coefficient of friction decreases and then increases. The optimum values, 2.816×10^{-4} mm^3/N m and 0.437, respectively, are obtained for an energy density of 172 J/mm^3. The

Table 5 Corrosion properties of the 420 stainless steel produced by different manufacturing processes (*t*–layer thickness)

Condition		Corrosion current (µA/cm^2)	Breakdown potential (V)	Polarisation resistance (Ω/cm^2)	Corrosion rate (µm/year)
LPBF	*t*10 µm [89]	3.1	---	16,800	31
	*t*20 µm [89]	2.9	0.05	17,100	28
	*t*30 µm [89]	4.1	---	16,100	42
LPBF (*t*20 µm) (HT) [89, 91]		3.5	0.22	16,800	35
LPBF_fine powders (*t*20 µm) [86]		2.8	0.25	17,420	26
LPBF_fine powders (*t*20 µm) (HT) [86]		3.3	0.20	17,070	32
(Nb + Mo) LPBF (*t*20 µm) [93]		1.5	0.03	24,200	16
(Nb + Mo) LPBF (*t*20 µm) (HT) [93]		1.8	0.20	23,800	18
Wrought (quenched and tempered) [86, 93]		2.1	0.15	18,700	23

COF: 0.818 || Specific wear rate: 8.166×10^{-4} mm³/N.m

(a)

COF: 0.713 || Specific wear rate: 5.414×10^{-4} mm³/N.m

(b)

COF: 0.437 || Specific wear rate: 2.816×10^{-4} mm³/N.m

(c)

COF: 0.669 || Specific wear rate: 4.535×10^{-4} mm³/N.m

(d)

Fig. 15 Surface morphology of the wear tracks, COF and specific wear rate values for samples produced with energy densities of: **a** 125, **b** 148, **c** 172, and **d** 203 J/mm.³ (adapted from [108])

best results come from a combination of high densification and fine grain size.

For P20 steel, Lin et al. [120] (load of 5 kg and 600 rpm for 20 min; counter-body: tungsten balls) report two important points: (i) the defects on the surface can be beneficial for tribological properties because they can act as a reservoir for wear debris, minimising third body abrasion, and (ii) the metal matrix composites, and particularly hard particles, improve the wear resistance and lubrification of the base material.

4.7 Thermal properties

The thermal properties, particularly thermal conductivity, are the key aspect in the plastic injection mould industry since one of the great challenges of this industry is to make cooling more efficient, decreasing the total cycle time [29, 36].

The thermal properties of 420 stainless steel produced by LPBF have been little explored. Momenzadeh et al. [92] claimed that lower values for the layer thickness

Fig. 16 Thermal properties of as-built H13 steel ($P = 172$ W, $v = 700$ mm/s, $h = 80$ μm, $t = 30$ μm) as a function of temperature (adapted from [109])
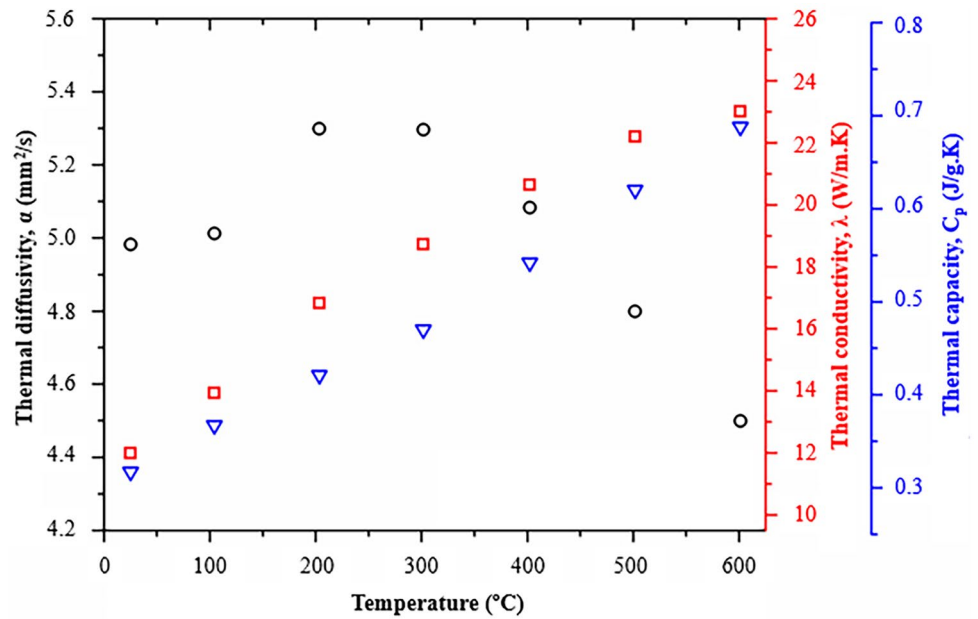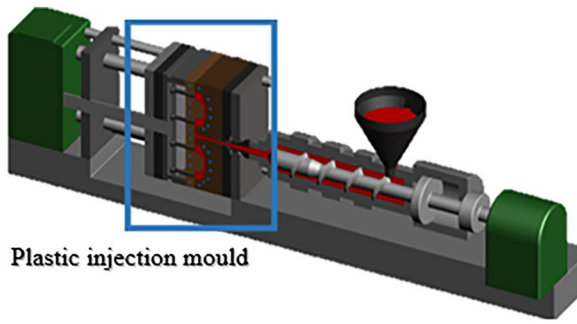

lead to higher coefficients of thermal expansion for temperatures above 100 °C but do not present any explanation for this result. However, since the density of the part produced where the layer is 10 μm thick (7.70 ± 0.02 g/cm³) was higher than that of the one with a thickness of 20 μm (7.67 ± 0.02 g/cm³) it can be affirmed that for the

processing parameters used by the authors, the porosity increased with the increase in the layer's thickness. Therefore, the higher the porosity is, the lower the thermal conductivity and the coefficient of thermal expansion are. For temperatures with the same limit, the addition of Nb and Mo to 420 stainless steel demonstrated a lower value of this
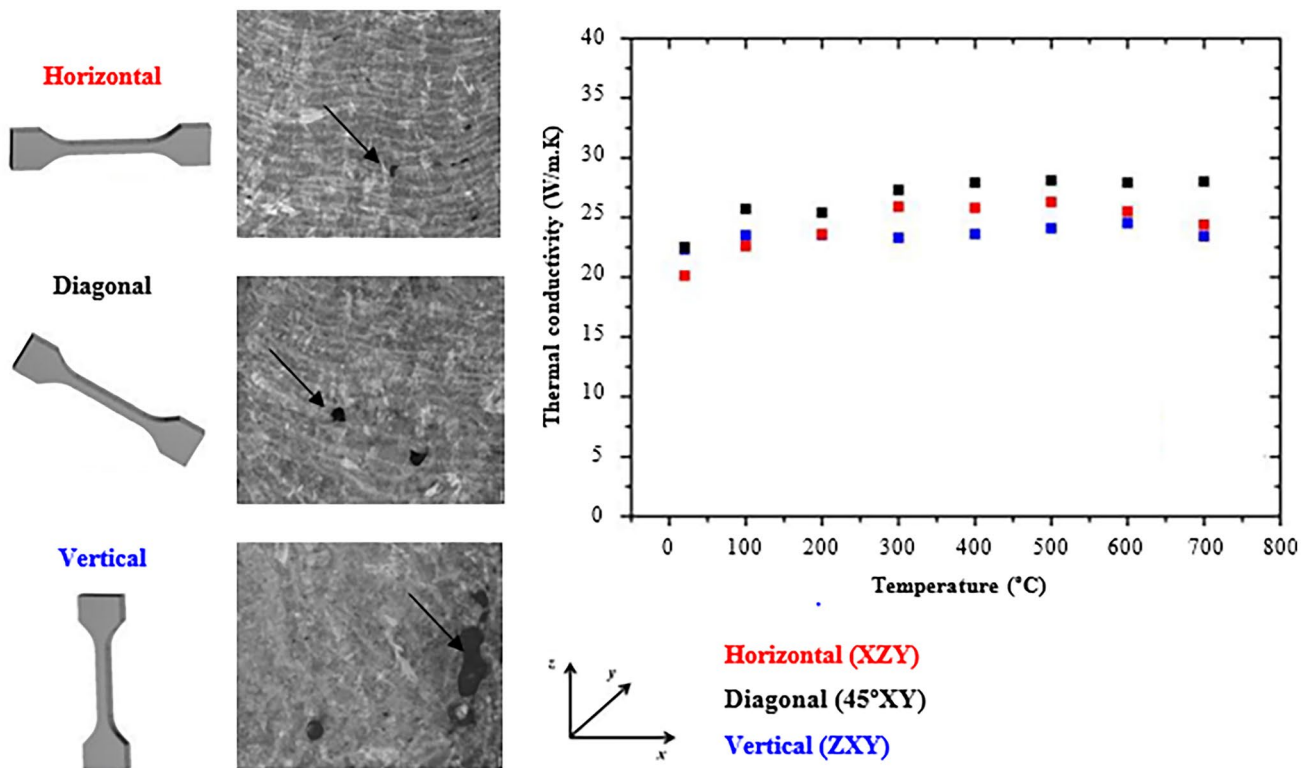
Fig. 17 Imperfections on the surface and thermal conductivity of the as-built H13 steel for three different build directions (based on [118])
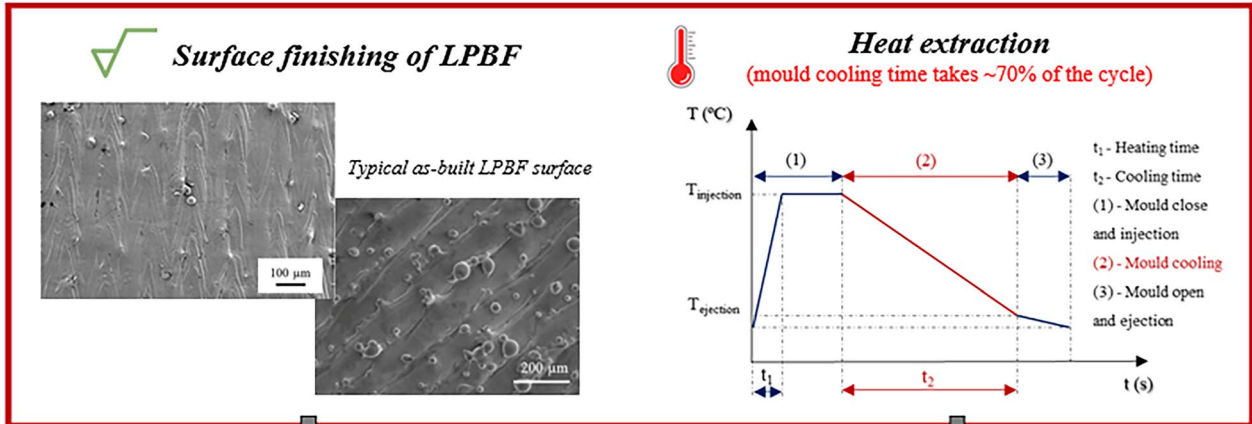
Fig. 18 Schematic representation of the limitations and potential solutions for the plastic injection mould industry

coefficient, reducing the possible warping that might occur in parts produced by LPBF.

Concerning H13 steel, Fonseca et al. [109] and Džugan et al. [118] mention that the thermal properties (thermal diffusivity, thermal conductivity, and thermal capacity) can be very sensitive to an increase in temperature (Fig. 16) and, therefore, the temperature of the platform influences these properties.

Džugan et al. [118] showed that the building directions do not influence the coefficient of thermal expansion. The values of thermal diffusivity and specific heat do not differ significantly up to 700 °C. However, the lower thermal conductivity

corresponds to the sample where the angle with the *z*-axis is 0° (vertical direction) (Fig. 17). This can be explained by the higher number of microstructural imperfections.

5 Challenges and future perspectives

LPBF investigations of the steels used in the plastic injection mould industry, as reviewed in the present article, are interdisciplinary since they integrate fields from materials science, metallurgical engineering, mechanical engineering to laser technology.

Despite the huge potential of LPBFed steel parts for the plastic injection moulding industry, there are two main aspects that need further investigation and optimization to make LPBFed solutions proper to mass plastic injection moulds production: surface finishing and heat extraction. Figure 18 aims to schematically explain the present limitations and the potential solutions for this purpose. Furthermore, the plastic injection moulds usually comprise very complex shape designs, and so the effects of the anisotropy and response of the steel alloys under multi-axial stresses can generate severe stress concentrations zones. In this regard, the integration of laser localised heat treatments with LPBF technology can be an effective strategy to investigate in short-coming studies. Moreover, the same strategy can be used to relieve the residual stresses generated on the surface. Finally, the optimization of the scanning strategy according to the specific and local demands of the plastic injection moulds to create a more customised component according to the requests is an added value to this industry.

5.1 Surface finishing

Surface finishing remains one of the LPBF technology's greatest challenges since it affects the appearance of the final product. The development of an adaptive process with the integration of other technologies (additive and subtractive operations), as well as the use of laser to reduce surface roughness must be adopted. The literature has already shown the suitability of CO_2 laser to polish the as-built surface of LPBF parts [159]. Another relevant aspect is the ability to monitor the in situ LPBF process is a priority area of study in the plastic injection moulding since each mould region is mechanically requested in a different way. In this sense, the in situ analysis of the properties is essential to adjust the LPBF processing parameters according to the local specifications of the part.

5.2 Heat extraction

The thermal properties of the steels used in the plastic injection mould industry produced by LPBF have not been much explored. However, considering that the cooling time of a mould is critical (~ 70% of the cycle) in the injection moulding process (as can be seen in the plot in Fig. 18), the development of solutions capable of promoting heat extraction is essential. The use of LPBF technique for combining different materials in the same parts, and thus creating multi-functional solutions not possible using conventional routes, might be a future possible strategy to improve this aspect. These multi-material solutions can be manufactured using hybrid additive manufacturing equipment (additive and subtractive operations in the same processing route) for obtaining high-advanced LPBFed solutions. Chen et al.

[160] have already proved to be possible the fabrication of the 316L stainless steel-CuSn10 multi-material structures by LPBF, which is a strong evidence of the potential of multi-material structures. Following this strategy, moulds with superior heat extraction can be manufactured by printing zones with high thermal conductivity materials (such as copper or copper alloys) within a steel block which allows assuring mechanical, corrosion and wear resistance, high dimensional and geometric accuracy, simultaneously.

6 Concluding remarks

This review provided an engineering overview concerning the response of 420 stainless steel, H13 and P20 steel parts made by Laser Powder Bed Fusion and the influence of the LPBF processing parameters on the final properties of these materials. The main conclusions are summarised as follows:

- H13 steel is the most studied steel (between these three steels considered) concerning the production of metallic LPBFed parts. Contrarily, P20 steel has not been studied much yet.
- An increase in the LPBF energy density is beneficial as it increases densification, with optimum values of 53, 60, and 79 J/mm^3 for 420 stainless steel, H13, and P20 steels, respectively. Subsequent heat treatments have a positive effect on this property.
- Surface roughness of the parts produced is a poorly explored property in the studies of this review. The surface roughness of 420 stainless steel parts increases with increasing layer thickness and laser spot size. For the same processing parameters and considered aspects, the addition of alloying elements does not appear to have any influence on the surface roughness of LPBFed parts of this steel.
- Considerable variability in the mechanical properties has been reported. This variability, at least partially, originates from the sensitivity on the properties of these materials to LPBF process parameters, which are still not fully understood. The mechanical properties of the as-built parts are strongly influenced by the energy density and the resulting microstructural properties. The mechanical strength and hardness of the LPBFed 420 stainless steel parts are superior to that of wrought materials, MIM parts, and annealed cold drawn ones, but the elongation tends to be lower. The addition of Nb and Mo improves the mechanical behaviour of this steel. The hardness of the H13 parts is related to the strain rate and the mechanical strength depends on the build direction; after heat treatment, higher values of yield strength, ultimate tensile strength, and elongation are reported. For P20 steel, the hardness of LPBFed parts is higher than the one of con-

ventional processes. The fatigue life of LPBFed H13 steel parts is inferior to that of parts fabricated by conventional methods. No fatigue resistance results are presented for 420 stainless steel and P20 steel in the articles considered in this review.

- The corrosion properties of the parts depend on the microstructure, porosity, and chemical composition of the material. For 420 stainless steel, the presence of chromium allows the formation of a chromium oxide passive film and inhibits surface corrosion; the addition of Nb and Mo is beneficial for these properties. Subsequent heat treatments do not have a significant effect on the corrosion properties of 420 stainless steel parts. LPBFed P20 steel parts showed poorer corrosion resistance compared with heat-treated ones. No results could be found for LPBFed H13 steel parts.

- The tribological properties of the parts are dependent on the microstructure, porosity, and surface roughness. The wear resistance of the materials processed by LPBF is higher compared to traditional manufacturing processes. No tribological results are reported for LPBFed 420 stainless steel parts. For H13 steel, the best tribological properties are obtained from the combination of high densification and fine grain size. Concerning the addressed studies on P20 steel parts, the defects on the surface resulting from the LPBF process are beneficial for the tribological properties because they can act as a reservoir for wear debris, minimising any third body abrasion.

- The thermal properties of the LPBFed parts have been little studied. For 420 stainless steel, a reduction in the layer thickness leads to higher values of the coefficient of thermal expansion. The addition of Nb and Mo has the opposite effect, reducing any possible warping. Concerning H13 steel, the thermal properties are very sensitive to an increase in temperature, namely of the platform. The building direction affects the thermal conductivity, due to the difference in terms of microstructural imperfections.

- It is important to highlight that there is a panoply of aspects, essential in the LPBF process and in the final properties of the components, rarely mentioned in the studies considered in this review, such as protective gas flow during production, type, height and temperature of the supports, dimensional compensations, and overmelting between passages and layers. To further advance the fundamental understanding of the process-structure–property relationship, deep theoretical investigations related to physical and chemical metallurgy and multiphysics simulation are required. This would make understanding the melt pool characteristics, residual stresses and distortion, densification, phase transformations, among others possible to predict the build properties or customise the parts, taking into consideration the required properties.

Author contribution Ângela Cunha: methodology, investigation, writing–original draft. Ana Marques: investigation, writing–review & editing. Mariana Rodrigues Silva: writing–review & editing. Flávio Bartolomeu: writing–review & editing. Filipe Samuel Silva: supervision, writing–review & editing. Michael Gasik: writing–review and editing. Bruno Trindade: conceptualization, validation, writing–review & editing. Óscar Carvalho: conceptualization, supervision, writing–review & editing.

Data availability All data used in this work have been properly cited within the article.

Code availability Not applicable.

Declarations

Ethics approval Not applicable.

Consent to participate The authors declare that all authors have approved the manuscript and agree with its submission to IJAMT.

Consent for publication The authors declare that all authors agree to sign the transfer of copyright for the publisher to publish this article upon on acceptance.

Conflict of interest The authors declare no competing interests.

References

1. Haghdadi N, Laleh M, Moyle M, Primig S (2021) Additive manufacturing of steels: a review of achievements and challenges. J Mater Sci 56:64–107. https://doi.org/10.1007/s10853-020-05109-0

2. Khairallah SA, Anderson AT, Rubenchik A, King WE (2016) Laser powder-bed fusion additive manufacturing: Physics of complex melt flow and formation mechanisms of pores, spatter, and denudation zones. Acta Mater 108:36–45. https://doi.org/10.1016/j.actamat.2016.02.014

3. Herzog D, Seyda V, Wycisk E, Emmelmann C (2016) Additive manufacturing of metals. Acta Mater 117:371–392. https://doi.org/10.1016/j.actamat.2016.07.019

4. Gu DD, Meiners W, Wissenbach K, Poprawe R (2012) Laser additive manufacturing of metallic components: materials, processes and mechanisms. Int Mater Rev 57:133–164. https://doi.org/10.1179/1743280411Y.0000000014

5. DebRoy T, Wei HL, Zuback JS et al (2018) Additive manufacturing of metallic components - process, structure and properties. Prog Mater Sci 92:112–224. https://doi.org/10.1016/j.pmatsci.2017.10.001

6. Emmelmann C, Kranz J, Herzog D, Wycisk E (2013) Laser Additive Manufacturing of Metals. In: V. S, M. B (eds) Laser Technology in Biomimetics: Basics and Applications. Springer, Berlin, Heidelberg, pp 143–162

7. Wang J, Liu S, Fang Y, He Z (2020) A short review on selective laser melting of H13 steel. Int J Adv Manuf Technol 108:2453–2466. https://doi.org/10.1007/s00170-020-05584-4

8. Zhang LC, Attar H, Calin M, Eckert J (2016) Review on manufacture by selective laser melting and properties of titanium based materials for biomedical applications. Mater Technol 31:66–76. https://doi.org/10.1179/1753555715Y.0000000076

9. Jiang J, Xu X, Stringer J (2018) Support structures for additive manufacturing: A review. J Manuf Mater Process. https://doi.org/10.3390/jmmp2040064

10. Jiang J, Ma Y (2020) Path planning strategies to optimize accuracy, quality, build time and material use in additive manufacturing: a review. Micromachines. https://doi.org/10.3390/MI11070633

11. Jiang J, Xiong Y, Zhang Z, Rosen DW (2022) Machine learning integrated design for additive manufacturing. J Intell Manuf 33:1073–1086. https://doi.org/10.1007/s10845-020-01715-6

12. Busachi A, Erkoyuncu J, Colegrove P et al (2017) A review of additive manufacturing technology and cost estimation techniques for the defence sector. CIRP J Manuf Sci Technol 19:117–128. https://doi.org/10.1016/j.cirpj.2017.07.001

13. Mazur M, Leary M, McMillan M et al (2016) SLM additive manufacture of H13 tool steel with conformal cooling and structural lattices. Rapid Prototyp J 22:504–518. https://doi.org/10.1108/RPJ-06-2014-0075

14. Hosseini E, Popovich VA (2019) A review of mechanical properties of additively manufactured Inconel 718. Addit Manuf 30:100877. https://doi.org/10.1016/j.addma.2019.100877

15. Yan JJ, Chen MT, Quach WM et al (2019) Mechanical properties and cross-sectional behavior of additively manufactured high strength steel tubular sections. Thin-Walled Struct 144:106158. https://doi.org/10.1016/j.tws.2019.04.050

16. Bartolomeu F, Costa MM, Alves N et al (2020) Additive manufacturing of NiTi-Ti6Al4V multi-material cellular structures targeting orthopedic implants. Opt Lasers Eng 134:106208. https://doi.org/10.1016/j.optlaseng.2020.106208

17. Singh R, Singh S (2017) Additive manufacturing: an overview. In: Reference Module in Materials Science and Materials Engineering, pp 1–12

18. Frazier WE (2014) Metal additive manufacturing: A review. J Mater Eng Perform 23:1917–1928. https://doi.org/10.1007/s11665-014-0958-z

19. Zhang J, Song B, Wei Q et al (2019) A review of selective laser melting of aluminum alloys: processing, microstructure, property and developing trends. J Mater Sci Technol 35:270–284. https://doi.org/10.1016/j.jmst.2018.09.004

20. Yap CY, Chua CK, Dong ZL et al (2015) Review of selective laser melting: Materials and applications. Appl Phys Rev. https://doi.org/10.1063/1.4935926

21. Aboulkhair NT, Simonelli M, Parry L et al (2019) 3D printing of aluminium alloys: additive manufacturing of aluminium alloys using selective laser melting. Prog Mater Sci 106:100578. https://doi.org/10.1016/j.pmatsci.2019.100578

22. Bartolomeu F, Faria S, Carvalho O et al (2016) Predictive models for physical and mechanical properties of Ti6Al4V produced by Selective Laser Melting. Mater Sci Eng A 663:181–192. https://doi.org/10.1016/j.msea.2016.03.113

23. Liu Y, Yang Y, Mai S et al (2015) Investigation into spatter behavior during selective laser melting of AISI 316L stainless steel powder. Mater Des 87:797–806. https://doi.org/10.1016/j.matdes.2015.08.086

24. Prashanth KG (2020) Selective laser melting: Materials and applications. J Manuf Mater Process 4:15–17. https://doi.org/10.3390/jmmp4010013

25. Song X, Zhai W, Huang R et al (2021) Metal-Based 3D-Printed micro parts & structures. In: Encyclopedia of Materials: Metals and Alloys. pp 448–461

26. Miranda G, Faria S, Bartolomeu F et al (2016) Predictive models for physical and mechanical properties of 316L stainless steel produced by selective laser melting. Mater Sci Eng A 657:43–56. https://doi.org/10.1016/j.msea.2016.01.028

27. Ali MAM, Idayu N, Abduallah Z et al (2017) Interchangeable core and cavity plates for two-plate family injection mould. J Mech Eng Sci 11:2815–2824. https://doi.org/10.15282/jmes.11.3.2017.4.0255

28. Raus AA, Wahab MS, Ibrahim MHI et al (2017) A comparative study of mould base tool materials in plastic injection moulding to improve cycle time and warpage using statistical method. J Mech Eng SI 4:1–17

29. Kitayama S, Yokoyama M, Takano M, Aiba S (2017) Multi-objective optimization of variable packing pressure profile and process parameters in plastic injection molding for minimizing warpage and cycle time. Int J Adv Manuf Technol 92:3991–3999. https://doi.org/10.1007/s00170-017-0456-1

30. Alkaabneh FA, Barghash M, Mishael I (2013) A combined analytical hierarchical process (AHP) and Taguchi experimental design (TED) for plastic injection molding process settings. Int J Adv Manuf Technol 66:679–694. https://doi.org/10.1007/s00170-012-4357-z

31. Zabala B, Fernandez X, Rodriguez JC et al (2019) Mechanism-based wear models for plastic injection moulds. Wear 440–441:203105. https://doi.org/10.1016/j.wear.2019.203105

32. Low MLH, Lee KS (2003) A parametric-controlled cavity layout design system for a plastic injection mould. Int J Adv Manuf Technol 21:807–819. https://doi.org/10.1007/s00170-002-1397-9

33. Öztürk O, Onmuş O, Williamson DL (2005) Microstructural, mechanical, and corrosion characterization of plasma-nitrided plastic injection mould steel. Surf Coat Technol 196:341–348. https://doi.org/10.1016/j.surfcoat.2004.08.154

34. Dang X-P, Park H-S (2011) Design of U-shape milled groove conformal cooling channels for plastic injection mold. Int J Precis Eng Manuf 12:73–84. https://doi.org/10.1007/s12541-011-0009-8

35. Park H-S, Dang X-P (2017) Development of a smart plastic injection mold with conformal cooling channels. Procedia Manuf 10:48–59. https://doi.org/10.1016/j.promfg.2017.07.020

36. Jahan SA, El-mounayri H (2018) A thermomechanical analysis of conformal cooling channels in 3D printed plastic injection molds. Appl Sci 8:2567. https://doi.org/10.3390/app8122567

37. Dimla DE, Camilotto M, Miani F (2005) Design and optimisation of conformal cooling channels in injection moulding tools. J Mater Process Technol 164–165:1294–1300. https://doi.org/10.1016/j.jmatprotec.2005.02.162

38. Au KM, Yu KM (2007) A scaffolding architecture for conformal cooling design in rapid plastic injection moulding. Int J Adv Manuf Technol 34:496–515. https://doi.org/10.1007/s00170-006-0628-x

39. Phull GS, Kumar S, Walia RS (2018) Conformal cooling for molds produced by additive manufacturing: a review. Int J Mech Eng Technol 9:1162–1172

40. Jahan SA, El-Mounayri H (2016) Optimal conformal cooling channels in 3D printed dies for plastic injection molding. Procedia Manuf 5:888–900. https://doi.org/10.1016/j.promfg.2016.08.076

41. Saifullah ABM, Masood SH, Nikzad M (2016) an investigation on fabrication of conformal cooling channel with direct metal deposition for injection moulding. Elsevier Ltd

42. Jahan S, Wu T, Shin Y et al (2019) Thermo-fluid topology optimization and experimental study of conformal cooling channels for 3D printed plastic injection molds. Procedia Manuf 34:631–639. https://doi.org/10.1016/j.promfg.2019.06.120

43. El KMF, Rennie AEW, Ghazy M (2019) Tool life performance of injection mould tooling fabricated by selective laser melting for high-volume production. Materials (Basel) 12:1–23. https://doi.org/10.3390/ma12233910

44. Jahan SA, Wu T, Zhang Y et al (2017) Thermo-mechanical design optimization of conformal cooling channels using design of experiments approach. Procedia Manuf 10:898–911. https://doi.org/10.1016/j.promfg.2017.07.078

45. Papageorgiou D, Medrea C, Kyriakou N (2013) Failure analysis of H13 working die used in plastic injection moulding. Eng Fail Anal 35:355–359. https://doi.org/10.1016/j.engfailanal.2013.02.028

46. Mendible G, Rulander J, Johnston S (2017) Comparative study of rapid and conventional tooling for plastics injection molding. Rapid Prototyp J 23:344–352. https://doi.org/10.1108/RPJ-01-2016-0013

47. Martínez-Mateo I, Carrión-Vilches FJ, Sanes J, Bermúdez MD (2011) Surface damage of mold steel and its influence on surface roughness of injection molded plastic parts. Wear 271:2512–2516. https://doi.org/10.1016/j.wear.2010.11.054

48. Firrao D, Matteis P, Spena PR, Gerosa R (2013) Influence of the microstructure on fatigue and fracture toughness properties of large heat-treated mold steels. Mater Sci Eng A 559:371–383. https://doi.org/10.1016/j.msea.2012.08.113

49. Menges G, Michaeli W, Mohren P (2001) How to make injection molds, 3rd edn. Carl Hanser Verlag GmbH & Co, KG

50. Yadroitsev I, Krakhmalev P, Yadroitsava I (2015) Hierarchical design principles of selective laser melting for high quality metallic objects. Addit Manuf 7:45–56. https://doi.org/10.1016/j.addma.2014.12.007

51. Rosato DV, Rosato MG, Rosato DV (2000) Injection Molding Handbook. Kluwer Academic Publisher

52. Mennig G, Stoeckhert K (2013) Mold-Making Handbook, 3rd edn. Hanser Publishers, Munich

53. Zhao X, Wei Q, Song B et al (2015) Fabrication and characterization of AISI 420 stainless steel using selective laser melting. Mater Manuf Process 30:1283–1289. https://doi.org/10.1080/10426914.2015.1026351

54. Li S, Liu Y, Tian Z et al (2020) Biomimetic superhydrophobic and antibacterial stainless-steel mesh via double-potentiostatic electrodeposition and modification. Surf Coatings Technol 403:126355. https://doi.org/10.1016/j.surfcoat.2020.126355

55. Nachum S, Fleck NA (2011) The microstructure and mechanical properties of ball-milled stainless steel powder: the effect of hot-pressing vs. laser sintering. Acta Mater 59:7300–7310. https://doi.org/10.1016/j.actamat.2011.08.004

56. Todorov T, Todorov G, Romanov B (2019) Design and simulation of mould tools with multi-material structure for plastic injection moulding based on additive technology. In: 2019 International Conference on Creative Business for Smart and Sustainable Growth (CREBUS). IEEE, pp 1–6

57. Mazur M, Brincat P, Leary M, Brandt M (2017) Numerical and experimental evaluation of a conformally cooled H13 steel injection mould manufactured with selective laser melting. Int J Adv Manuf Technol 93:881–900. https://doi.org/10.1007/s00170-017-0426-7

58. Chen J, Conlon K, Xue L, Rogge R (2010) Experimental study of residual stresses in laser clad AISI P20 tool steel on pre-hardened wrought P20 substrate. Mater Sci Eng A 527:7265–7273. https://doi.org/10.1016/j.msea.2010.07.098

59. Kapil S, Legesse F, Negi S et al (2020) Hybrid layered manufacturing of a bimetallic injection mold of P20 tool steel and mild steel with conformal cooling channels. Prog Addit Manuf. https://doi.org/10.1007/s40964-020-00129-3

60. Ding D, Pan Z, Cuiuri D, Li H (2015) Wire-feed additive manufacturing of metal components: technologies, developments and future interests. Int J Adv Manuf Technol 81:465–481. https://doi.org/10.1007/s00170-015-7077-3

61. Song B, Zhao X, Li S et al (2015) Differences in microstructure and properties between selective laser melting and traditional manufacturing for fabrication of metal parts: A review. Front Mech Eng 10:111–125. https://doi.org/10.1007/s11465-015-0341-2

62. Leitz K, Singer P, Plankensteiner A et al (2017) Multi-physical simulation of selective laser melting. Met Powder Rep 72:331–338. https://doi.org/10.1016/j.mprp.2016.04.004

63. Vock S, Klöden B, Kirchner A et al (2019) Powders for powder bed fusion: a review. Prog Addit Manuf 4:383–397. https://doi.org/10.1007/s40964-019-00078-6

64. Telasang G, Dutta Majumdar J, Padmanabham G et al (2014) Effect of laser parameters on microstructure and hardness of laser clad and tempered AISI H13 tool steel. Surf Coatings Technol 258:1108–1118. https://doi.org/10.1016/j.surfcoat.2014.07.023

65. Zhou X, Liu X, Zhang D et al (2015) Balling phenomena in selective laser melted tungsten. J Mater Process Technol 222:33–42. https://doi.org/10.1016/j.jmatprotec.2015.02.032

66. Narvan M, Al-Rubaie KS, Elbestawi M (2019) Process-structure-property relationships of AISI H13 tool steel processed with selective laser melting. Materials (Basel) 12:1–20. https://doi.org/10.3390/ma12142284

67. Carlton HD, Haboub A, Gallegos GF et al (2016) Damage evolution and failure mechanisms in additively manufactured stainless steel. Mater Sci Eng A 651:406–414. https://doi.org/10.1016/j.msea.2015.10.073

68. Lee J, Choe J, Park J et al (2019) Microstructural effects on the tensile and fracture behavior of selective laser melted H13 tool steel under varying conditions. Mater Charact 155:109817. https://doi.org/10.1016/j.matchar.2019.109817

69. Katancik M, Mirzababaei S, Ghayoor M, Pasebani S (2020) Selective laser melting and tempering of H13 tool steel for rapid tooling applications. J Alloys Compd 849:156319. https://doi.org/10.1016/j.jallcom.2020.156319

70. Pauzon C, Hryha E, Forêt P, Nyborg L (2019) Effect of argon and nitrogen atmospheres on the properties of stainless steel 316 L parts produced by laser-powder bed fusion. Mater Des. https://doi.org/10.1016/j.matdes.2019.107873

71. Gokuldoss PK, Kolla S, Eckert J (2017) Additive manufacturing processes: Selective laser melting, electron beam melting and binder jetting-selection guidelines. Materials (Basel). https://doi.org/10.3390/ma10060672

72. Sander J, Hufenbach J, Giebeler L et al (2016) Microstructure and properties of FeCrMoVC tool steel produced by selective laser melting. Mater Des 89:335–341. https://doi.org/10.1016/j.matdes.2015.09.148

73. Kempen K, Vrancken B, Buls S et al (2014) Selective laser melting of crack-free high density M2 high speed steel parts by baseplate preheating. J Manuf Sci Eng Trans ASME 136:1–7. https://doi.org/10.1115/1.4028513

74. Tomas J, Hitzler L, Köller M et al (2020) The dimensional accuracy of thin-walled parts manufactured by laser-powder bed fusion process. J Manuf Mater Process 4:12. https://doi.org/10.3390/JMMP4030091

75. Gu D, Guo M, Zhang H et al (2020) Effects of laser scanning strategies on selective laser melting of pure tungsten. Int J Extrem Manuf. https://doi.org/10.1088/2631-7990/ab7b00

76. Jia H, Sun H, Wang H et al (2021) Scanning strategy in selective laser melting (SLM): a review. Int J Adv Manuf Technol 113:2413–2435. https://doi.org/10.1007/s00170-021-06810-3

77. Zhang W, Tong M, Harrison NM (2020) Scanning strategies effect on temperature, residual stress and deformation by multi-laser beam powder bed fusion manufacturing. Addit Manuf 36:101507. https://doi.org/10.1016/j.addma.2020.101507

78. Robinson J, Ashton I, Fox P et al (2018) Determination of the effect of scan strategy on residual stress in laser powder bed fusion additive manufacturing. Addit Manuf 23:13–24. https://doi.org/10.1016/j.addma.2018.07.001

79. Thijs L, Verhaeghe F, Craeghs T et al (2010) A study of the microstructural evolution during selective laser melting of Ti-6Al-4V. Acta Mater 58:3303–3312. https://doi.org/10.1016/j.actamat.2010.02.004

80. Masoomi M, Thompson SM, Shamsaei N (2017) Laser powder bed fusion of Ti-6Al-4V parts: thermal modeling and mechanical implications. Int J Mach Tools Manuf 118–119:73–90. https://doi.org/10.1016/j.ijmachtools.2017.04.007

81. Valente EH, Gundlach C, Christiansen TL, Somers MAJ (2019) Effect of scanning strategy during selective laser melting on surface topography, porosity, and microstructure of additively manufactured Ti-6Al-4V. Appl Sci. https://doi.org/10.3390/app9245554

82. Jhabvala J, Boillat E, Antignac T, Glardon R (2010) On the effect of scanning strategies in the selective laser melting process. Virtual Phys Prototyp 5:99–109. https://doi.org/10.1080/17452751003688368

83. Sames WJ, List FA, Pannala S et al (2016) The metallurgy and processing science of metal additive manufacturing. Int Mater Rev 61:315–360. https://doi.org/10.1080/09506608.2015.1116649

84. Yang XH, Jiang CM, Ho JR et al (2021) Effects of laser spot size on the mechanical properties of AISI 420 stainless steel fabricated by selective laser melting. Materials (Basel). https://doi.org/10.3390/ma14164593

85. Tian Y, Chadha K, Aranas C (2021) Laser powder bed fusion of ultra-high-strength 420 stainless steel: Microstructure characterization, texture evolution and mechanical properties. Mater Sci Eng A 805:140790. https://doi.org/10.1016/j.msea.2021.140790

86. Nath SD, Okello A, Kelkar R et al (2021) Adapting L-PBF process for fine powders: a case study in 420 stainless steel. Mater Manuf Process 1–12. https://doi.org/10.1080/10426914.2021.1885707

87. Shen LC, Yang XH, Ho JR et al (2020) Effects of build direction on the mechanical properties of a martensitic stainless steel fabricated by selective laser melting. Materials (Basel) 13:1–18. https://doi.org/10.3390/ma13225142

88. Shi Y, Xiong X, Liu Z et al (2020) Mechanical property evaluation of a slmed martensitic stainless steel. Acta Metall Sin 33:1466–1476. https://doi.org/10.1007/s40195-020-01128-7

89. Nath SD, Gupta G, Kearns M et al (2020) Effects of layer thickness in laser-powder bed fusion of 420 stainless steel. Rapid Prototyp J 26:1197–1208. https://doi.org/10.1108/RPJ-10-2019-0279

90. Saeidi K, Zapata DL, Lofaj F et al (2019) Ultra-high strength martensitic 420 stainless steel with high ductility. Addit Manuf 29:100803. https://doi.org/10.1016/j.addma.2019.100803

91. Nath SD, Irrinki H, Gupta G et al (2019) Microstructure-property relationships of 420 stainless steel fabricated by laser-powder bed fusion. Powder Technol 343:738–746. https://doi.org/10.1016/j.powtec.2018.11.075

92. Momenzadeh N, Nath SD, Berfield TA, Atre SV (2019) In Situ Measurement of Thermal Strain Development in 420 Stainless Steel Additive Manufactured Metals. Exp Mech 59:819–827. https://doi.org/10.1007/s11340-019-00513-3

93. Nath SD, Clinning E, Gupta G et al (2019) Effects of Nb and Mo on the microstructure and properties of 420 stainless steel processed by laser-powder bed fusion. Addit Manuf 28:682–691. https://doi.org/10.1016/j.addma.2019.06.016

94. Krakhmalev P, Yadroitsava I, Fredriksson G, Yadroitsev I (2015) In situ heat treatment in selective laser melted martensitic AISI 420 stainless steels. Mater Des 87:380–385. https://doi.org/10.1016/j.matdes.2015.08.045

95. Wang M, Wu Y, Wei Q, Shi Y (2020) Thermal fatigue properties of H13 hot-work tool steels processed by selective laser melting. Metals (Basel) 10:1–17. https://doi.org/10.3390/met10010116

96. Ren B, Lu D, Zhou R et al (2019) Preparation and mechanical properties of selective laser melted H13 steel. J Mater Res 34:1415–1425. https://doi.org/10.1557/jmr.2019.10

97. Deirmina F, Peghini N, AlMangour B et al (2019) Heat treatment and properties of a hot work tool steel fabricated by additive manufacturing. Mater Sci Eng A 753:109–121. https://doi.org/10.1016/j.msea.2019.03.027

98. Wang M, Li W, Wu Y et al (2019) High-temperature properties and microstructural stability of the AISI H13 hot-work tool steel processed by selective laser melting. Metall Mater Trans B Process Metall Mater Process Sci 50:531–542. https://doi.org/10.1007/s11663-018-1442-1

99. Jung ID, Choe J, Yun J et al (2019) Dual speed laser re-melting for high densification in H13 tool steel metal 3D printing. Arch Metall Mater 64:571–578. https://doi.org/10.24425/amm.2019.127580

100. Deirmina F, AlMangour B, Grzesiak D, Pellizzari M (2018) H13–partially stabilized zirconia nanocomposites fabricated by high-energy mechanical milling and selective laser melting. Mater Des 146:286–297. https://doi.org/10.1016/j.matdes.2018.03.017

101. Ackermann M, Šafka J, Voleský L et al (2018) Impact testing of H13 tool steel processed with use of selective laser melting technology. Mater Sci Forum 919:43–51. https://doi.org/10.4028/www.scientific.net/MSF.919.43

102. Yan JJ, Zheng DL, Li HX et al (2017) Selective laser melting of H13: microstructure and residual stress. J Mater Sci 52:12476–12485. https://doi.org/10.1007/s10853-017-1380-3

103. AlMangour B, Grzesiak D, Yang JM (2016) Nanocrystalline TiC-reinforced H13 steel matrix nanocomposites fabricated by selective laser melting. Mater Des 96:150–161. https://doi.org/10.1016/j.matdes.2016.02.022

104. Narvan M, Ghasemi A, Fereiduni E et al (2021) Part deflection and residual stresses in laser powder bed fusion of H13 tool steel. Mater Des 204:109659. https://doi.org/10.1016/j.matdes.2021.109659

105. Kunz J, Herzog S, Kaletsch A, Broeckmann C (2021) Influence of initial defect density on mechanical properties of AISI H13 hot-work tool steel produced by laser powder bed fusion and hot isostatic pressing. Powder Metall. https://doi.org/10.1080/00325899.2021.1934634

106. Yonehara M, Ikeshoji TT, Nagahama T et al (2020) Parameter optimization of the high-power laser powder bed fusion process for H13 tool steel. Int J Adv Manuf Technol 110:427–437. https://doi.org/10.1007/s00170-020-05879-6

107. Pellizzari M, AlMangour B, Benedetti M et al (2020) Effects of building direction and defect sensitivity on the fatigue behavior of additively manufactured H13 tool steel. Theor Appl Fract Mech 108:102634. https://doi.org/10.1016/j.tafmec.2020.102634

108. Dzukey GA, Yang K, Wang Q et al (2020) Porosity, hardness, friction and wear performance analysis of H13 SLM-formed samples. J Mater Eng Perform 29:4957–4966. https://doi.org/10.1007/s11665-020-04999-0

109. Fonseca EB, Gabriel AHG, Araújo LC et al (2020) Assessment of laser power and scan speed influence on microstructural features and consolidation of AISI H13 tool steel processed by additive manufacturing. Addit Manuf 34:101250. https://doi.org/10.1016/j.addma.2020.101250

110. Pellizzari M, Furlani S, Deirmina F et al (2020) Fracture toughness of a hot work tool steel fabricated by laser-powder bed fusion additive manufacturing. Steel Res Int 91:1–7. https://doi.org/10.1002/srin.201900449

111. Zhao M, Duan C, Luo X (2020) Metallurgical defect behavior, microstructure evolution, and underlying thermal mechanisms of metallic parts fabricated by selective laser melting additive manufacturing. J Laser Appl 32:022012. https://doi.org/10.2351/1.5141074

112. Yan J, Song H, Dong Y et al (2020) High strength (~2000 MPa) or highly ductile (~11%) additively manufactured H13 by tempering at different conditions. Mater Sci Eng A 773:138845. https://doi.org/10.1016/j.msea.2019.138845

113. Garcias JF, Martins RF, Branco R et al (2021) Quasistatic and fatigue behavior of an AISI H13 steel obtained by additive manufacturing and conventional method. Fatigue Fract Eng Mater Struct 1–15. https://doi.org/10.1111/ffe.13565

114. Åsberg M, Fredriksson G, Hatami S et al (2019) Influence of post treatment on microstructure, porosity and mechanical properties of additive manufactured H13 tool steel. Mater Sci Eng A 742:584–589. https://doi.org/10.1016/j.msea.2018.08.046

115. Yan J, Zhou Y, Gu R et al (2019) A comprehensive study of steel powders (316L, H13, P20 and 18Ni300) for their selective laser melting additive manufacturing. Metals (Basel). https://doi.org/10.3390/met9010086

116. Körperich JP, Merkel M (2018) Thermographic analysis of the building height impact on the properties of tool steel in selective laser beam melting. Materwiss Werksttech 49:689–695. https://doi.org/10.1002/mawe.201800010

117. Krell J, Röttger A, Geenen K, Theisen W (2018) General investigations on processing tool steel X40CrMoV5-1 with selective laser melting. J Mater Process Technol 255:679–688. https://doi.org/10.1016/j.jmatprotec.2018.01.012

118. Džugan J, Halmešová K, Ackermann M et al (2020) Thermophysical properties investigation in relation to deposition orientation for SLM deposited H13 steel. Thermochim Acta 683:178479. https://doi.org/10.1016/j.tca.2019.178479

119. Nguyen VL, Kim EA, Lee SR et al (2018) Evaluation of Thermomechaate sensitivity of selective laser melted H13 tool steel using nanoindentation tests. Metals (Basel). https://doi.org/10.3390/met8080589

120. Lin Z, Zhang X, Ma F et al (2019) A research on the surface morphology, microstructure evolution and wear property of selective laser melting Al2O3/P20 composites. Mater Res Express 6:1265h3. https://doi.org/10.1088/2053-1591/ab691e

121. Li HX, Qi HL, Song CH et al (2018) Selective laser melting of P20 mould steel: investigation on the resultant microstructure, high-temperature hardness and corrosion resistance. Powder Metall 61:21–27. https://doi.org/10.1080/00325899.2017.1368965

122. Larimian T, Kannan M, Grzesiak D et al (2020) Effect of energy density and scanning strategy on densification, microstructure and mechanical properties of 316L stainless steel processed via selective laser melting. Mater Sci Eng A 770:138455. https://doi.org/10.1016/j.msea.2019.138455

123. Montero-Sistiaga ML, Godino-Martinez M, Boschmans K et al (2018) Microstructure evolution of 316L produced by HP-SLM (high power selective laser melting). Addit Manuf 23:402–410. https://doi.org/10.1016/j.addma.2018.08.028

124. Sadali MF, Hassan MZ, Ahmad F et al (2020) Influence of selective laser melting scanning speed parameter on the surface morphology, surface roughness, and micropores for manufactured Ti6Al4V parts. J Mater Res 35:2025–2035. https://doi.org/10.1557/jmr.2020.84

125. Dadbakhsh S, Hao L (2012) Effect of hot isostatic pressing (HIP) on Al composite parts made from laser consolidated Al/Fe 2O 3 powder mixtures. J Mater Process Technol 212:2474–2483. https://doi.org/10.1016/j.jmatprotec.2012.06.016

126. Simchi A, Asgharzadeh H (2004) Densification and microstructural evaluation during laser sintering of M2 high speed steel powder. Mater Sci Technol 20:1462–1468. https://doi.org/10.1179/026708304X3944

127. AlMangour B, Grzesiak D, Yang JM (2017) Selective laser melting of TiB2/H13 steel nanocomposites: influence of hot isostatic pressing post-treatment. J Mater Process Technol 244:344–353. https://doi.org/10.1016/j.jmatprotec.2017.01.019

128. Sun S, Brandt M, Easton M (2017) Powder bed fusion processes: an overview. In: Laser Additive Manufacturing: Materials, Design, Technologies, and Applications. pp 55–77

129. Hooper PA (2018) Melt pool temperature and cooling rates in laser powder bed fusion. Addit Manuf 22:548–559. https://doi.org/10.1016/j.addma.2018.05.032

130. Chen H, Gu D, Dai D et al (2017) Microstructure and composition homogeneity, tensile property, and underlying thermal physical mechanism of selective laser melting tool steel parts. Mater Sci Eng A 682:279–289. https://doi.org/10.1016/j.msea.2016.11.047

131. Law WK, Wong KC, Wang H et al (2021) Microstructure evolution in additively manufactured steel molds: a review. J Mater Eng Perform 30:6389–6405. https://doi.org/10.1007/s11665-021-05948-1

132. Brooks JW, Loretto MH, Smallman RE (1979) Direct observations of martensite nuclei in stainless steel. Acta Metall 27:1839–1847. https://doi.org/10.1016/0001-6160(79)90074-9

133. Reggiani B, Todaro I (2019) Investigation on the design of a novel selective laser melted insert for extrusion dies with conformal cooling channels. Int J Adv Manuf Technol 104:815–830. https://doi.org/10.1007/s00170-019-03879-9

134. Froend M, Ventzke V, Dorn F et al (2020) Microstructure by design: an approach of grain refinement and isotropy improvement in multi-layer wire-based laser metal deposition. Mater Sci Eng A 772:138635. https://doi.org/10.1016/j.msea.2019.138635

135. Chen H, Gu D, Dai D et al (2018) A novel approach to direct preparation of complete lath martensite microstructure in tool steel by selective laser melting. Mater Lett 227:128–131. https://doi.org/10.1016/j.matlet.2018.05.042

136. Kurzynowski T, Stopyra W, Gruber K et al (2019) Effect of scanning and support strategies on relative density of SLM-ed H13 steel in relation to specimen size. Materials (Basel). https://doi.org/10.3390/ma12020239

137. Gu D, Shen Y (2009) Balling phenomena in direct laser sintering of stainless steel powder: metallurgical mechanisms and control methods. Mater Des 30:2903–2910. https://doi.org/10.1016/j.matdes.2009.01.013

138. Kruth JP, Froyen L, Van Vaerenbergh J et al (2004) Selective laser melting of iron-based powder. J Mater Process Technol 149:616–622. https://doi.org/10.1016/j.jmatprotec.2003.11.051

139. Qiu C, Panwisawas C, Ward M et al (2015) On the role of melt flow into the surface structure and porosity development during selective laser melting. Acta Mater 96:72–79. https://doi.org/10.1016/j.actamat.2015.06.004

140. Simoni F, Huxol A, Villmer FJ (2021) Improving surface quality in selective laser melting based tool making. J Intell Manuf. https://doi.org/10.1007/s10845-021-01744-9

141. Leary M (2017) Surface roughness optimisation for selective laser melting (SLM): accommodating relevant and irrelevant surfaces. In: Brandt M (ed) Laser Additive Manufacturing: Materials, Design, Technologies, and Applications Materials, Design, Technologies, and Applications. Woodhead Publishing Series in Electronic and Optical Materials, pp 99–118

142. Agarwala M, Bourell D, Beaman J et al (1995) Direct selective laser sintering of metals. Rapid Prototyp J 1:26–36. https://doi.org/10.1108/13552549510078113

143. Wang L-Z, Wang S, Wu J-J (2017) Experimental investigation on densification behavior and surface roughness of AlSi10Mg

powders produced by selective laser melting. Opt Laser Technol 96:88–96. https://doi.org/10.1016/j.optlastec.2017.05.006

144. Ali H, Ghadbeigi H, Mumtaz K (2018) Effect of scanning strategies on residual stress and mechanical properties of selective laser melted Ti6Al4V. Mater Sci Eng A 712:175–187. https://doi.org/10.1016/j.msea.2017.11.103

145. Sealy MP, Hadidi H, Sotelo LD et al (2020) Compressive behavior of 420 stainless steel after asynchronous laser processing. CIRP Ann 69:169–172. https://doi.org/10.1016/j.cirp.2020.04.059

146. Brnic J, Turkalj G, Canadija M et al (2011) Martensitic stainless steel AISI 420 - mechanical properties, creep and fracture toughness. Mech Time-Dependent Mater 15:341–352. https://doi.org/10.1007/s11043-011-9137-x

147. Yan H, Bi H, Li X, Xu Z (2009) Precipitation and mechanical properties of Nb-modified ferritic stainless steel during isothermal aging. Mater Charact 60:204–209. https://doi.org/10.1016/j.matchar.2008.09.001

148. Sarkar S, Kumar CS, Nath AK (2019) Effects of different surface modifications on the fatigue life of selective laser melted 15–5 PH stainless steel. Mater Sci Eng A 762:138109. https://doi.org/10.1016/j.msea.2019.138109

149. Spierings AB, Starr TL, Wegener K (2013) Fatigue performance of additive manufactured metallic parts. Rapid Prototyp J 19:88–94. https://doi.org/10.1108/13552541311302932

150. Dörfert R, Zhang J, Clausen B et al (2019) Comparison of the fatigue strength between additively and conventionally fabricated tool steel 1.2344. Addit Manuf 27:217–223. https://doi.org/10.1016/j.addma.2019.01.010

151. Melia MA, Nguyen HDA, Rodelas JM, Schindelholz EJ (2019) Corrosion properties of 304L stainless steel made by directed energy deposition additive manufacturing. Corros Sci 152:20–30. https://doi.org/10.1016/j.corsci.2019.02.029

152. Schaller RF, Mishra A, Rodelas JM et al (2018) The Role of Microstructure and Surface Finish on the Corrosion of Selective Laser Melted 304L. J Electrochem Soc 165:C234–C242. https://doi.org/10.1149/2.0431805jes

153. Corengia P, Ybarra G, Moina C et al (2004) Microstructure and corrosion behaviour of DC-pulsed plasma nitrided AISI 410 martensitic stainless steel. Surf Coatings Technol 187:63–69. https://doi.org/10.1016/j.surfcoat.2004.01.031

154. Ko G, Kim W, Kwon K, Lee TK (2021) The corrosion of stainless steel made by additive manufacturing: a review. Metals (Basel) 11:1–21. https://doi.org/10.3390/met11030516

155. Hagen M (2000) Corrosion of steels. In: Materials Science and Technology: A Comprehensive Treatment: Corrosion and Environmental Degradation. R. W. Cahn, P. Haasen, E. J. Kramer, pp 1–68

156. Lorusso M (2019) Tribological and wear behavior of metal alloys produced by laser powder bed fusion (LPBF). In: Mohammad Asaduzzaman Chowdhury (ed) Friction, Lubrication and Wear. IntechOpen

157. Ralls AM, Kumar P, Menezes PL (2021) Tribological properties of additive manufactured materials for energy applications: a review. Processes 9:1–33. https://doi.org/10.3390/pr9010031

158. Liu Y, Zhai X, Deng Y, Wu D (2019) Tribological property of selective laser melting–processed 316L stainless steel against filled PEEK under water lubrication. Tribol Trans 62:962–970. https://doi.org/10.1080/10402004.2019.1635671

159. Obeidi MA, Mussatto A, Dogu MN et al (2022) Laser surface polishing of Ti-6Al-4V parts manufactured by laser powder bed fusion. Surf Coatings Technol 434:128179. https://doi.org/10.1016/j.surfcoat.2022.128179

160. Chen K, Wang C, Hong Q et al (2020) Selective laser melting 316L/CuSn10 multi-materials: processing optimization, interfacial characterization and mechanical property. J Mater Process Technol 283:116701. https://doi.org/10.1016/j.jmatprotec.2020.116701